

Serendipitous Discovery of Nine White Dwarfs with Gaseous Debris Disks

Carl Melis 1 , Beth Klein 2 , Alexandra E. Doyle 3 , Alycia Weinberger 4 , B. Zuckerman 2 , and Patrick Dufour 5 Center for Astrophysics and Space Sciences, University of California, San Diego, CA 92093-0424, USA; cmelis@ucsd.edu 2 Department of Physics and Astronomy, University of California, Los Angeles, CA 90095-1562, USA 3 Department of Earth, Planetary, and Space Sciences, University of California, Los Angeles, CA 90095, USA 4 Earth and Planets Laboratory, Carnegie Institution for Science, 5241 Broad Branch Road NW, Washington, DC 20015, USA 5 Département de Physique, Université de Montréal, Montréal, QC H3C 3J7, Canada Received 2020 August 31; revised 2020 September 29; accepted 2020 October 1; published 2020 December 11

Abstract

Optical spectroscopic observations of white dwarf stars selected from catalogs based on the Gaia DR2 database reveal nine new gaseous debris disks that orbit single white dwarf stars, about a factor of 2 increase over the previously known sample. For each source we present gas emission lines identified and basic stellar parameters, including abundances for lines seen with low-resolution spectroscopy. Principle discoveries include (1) the coolest white dwarf ($T_{\rm eff}\approx 12,720~{\rm K}$) with a gas disk; this star, WD0145+234, has been reported to have undergone a recent infrared outburst; (2) co-location in velocity space of gaseous emission from multiple elements, suggesting that different elements are well mixed; (3) highly asymmetric emission structures toward SDSS J0006+2858, and possibly asymmetric structures for two other systems; (4) an overall sample composed of approximately 25% DB and 75% DA white dwarfs, consistent with the overall distribution of primary atmospheric types found in the field population; and (5) never-before-seen emission lines from Na in the spectra of Gaia J0611-6931, semi-forbidden Mg, Ca, and Fe lines toward WD 0842+572, and Si in both stars. The currently known sample of gaseous debris disk systems is significantly skewed toward northern hemisphere stars, suggesting a dozen or so emission line stars are waiting to be found in the southern hemisphere.

Unified Astronomy Thesaurus concepts: Circumstellar matter (241); Exoplanet systems (484); Stellar abundances (1577); White dwarf stars (1799)

1. Introduction

The photospheres of white dwarf stars are "polluted" by remnant solid material from planetary systems that otherwise stably orbited their host star while it was on the main sequence (e.g., Zuckerman et al. 2007; Jura 2008; Farihi et al. 2009; Dufour et al. 2010; Klein et al. 2010; Melis et al. 2010; Gänsicke et al. 2012; Xu et al. 2013, and references therein). Prior to being accreted, this solid material must find its way into the host star's Roche radius and be tidally shredded into disks of dust and gas (e.g., Debes & Sigurdsson 2002; Jura 2003; Frewen & Hansen 2014; Vanderburg et al. 2015; Veras et al. 2016; Manser et al. 2019).

While the most heavily polluted white dwarf stars known are typically host to infrared excess emission and hence orbiting dust disks (e.g., Farihi 2016 and references therein), a subset of these objects additionally are host to disks of gaseous metallic material (Gänsicke et al. 2006, 2007, 2008; Melis et al. 2010, 2012; Brinkworth et al. 2012; Farihi et al. 2012; Hartmann et al. 2016; Manser et al. 2016a, 2016b, 2020; Xu et al. 2016). Models of disk formation and evolution suggest that dusty material is a necessary precondition to producing gaseous material in white dwarf debris disks. The gaseous material may form either from repeated impacts of solids within the dust disk or from sublimation of dusty material at the inner edge of the debris disk; the gas subsequently viscously spreads throughout the disk (e.g., Jura 2008; Melis et al. 2010; Bochkarev & Rafikov 2011; Hartmann et al. 2011, 2016; Rafikov 2011a, 2011b; Metzger et al. 2012; Bear & Soker 2013; Kenyon & Bromley 2017).

Gaseous material may act to aerodynamically drag dust particles, removing angular momentum and transporting them to the inner disk and eventually the star. Detailed study of dustand gas-disk components around single white dwarf stars can provide insight into the fate of solid material in planetary systems and hence what may very well happen to our own solar system billions of years from now (e.g., Debes & Sigurdsson 2002; Farihi et al. 2009; Frewen & Hansen 2014; Manser et al. 2016b; Veras et al. 2016; Xu et al. 2016; Cauley et al. 2018; Mustill et al. 2018; Grishin & Veras 2019; Malamud & Perets 2020; Maldonado et al. 2020a, 2020b). Additionally, intensive monitoring of gas-disk white dwarf stars can possibly provide a way to elucidate the size, density, and orbit of disintegrating rocky bodies around white dwarf stars; for example, what appears to be part of a core from a differentiated rocky object orbiting the heavily polluted star SDSS J1228 +1040 (Manser et al. 2019) and an intact gas giant planet being accreted by WD J091405.30+191412.25 (Gänsicke et al. 2019).

In this paper we report on the discovery of a set of nine new white dwarf stars that host gas-disk emission lines in their optical spectra. Included in this set is the recently reported infrared "outburst" object WD0145+234 (Wang et al. 2019). In addition to detection of gas-disk emission lines in this system (confirming it to be host to gaseous and dusty disk components), we also identify atmospheric pollution indicating that this material is being accreted by the host star. Below we describe our target selection strategy, observations conducted for newly discovered gas-disk systems, measurements made, target-specific discussion, and an overall sample discussion.

2. Target Selection and Observations

Stars were observed as part of a large-scale survey to identify the most heavily polluted white dwarfs through low-resolution optical spectroscopy. We began with the sample of Gentile Fusillo (2019), which reports the probability of an object being a white dwarf and stellar parameters (e.g., T_{eff} and $\log g$) based on fits to photometric data. These determinations are heavily informed by Gaia DR2 data, thus we refer to it as the "Gaia DR2 sample." Targets with evidence for infrared excess emission or having a helium-dominated atmosphere received higher priority for follow-up. Infrared excess emission data came from 2MASS, VISTA, and WISE (e.g., Xu et al. 2020), while GALEX colors were used to identify helium-dominated atmosphere white dwarfs (where available; helium-dominated atmosphere targets can have more readily identifiable atmospheric pollution at low spectral resolution than can hydrogendominated atmosphere objects). In this paper we do not assess the reality of any putative infrared excess emission detected for our target stars nor do we report on any infrared emission characteristics; this will be the subject of future work. In sum, we have observed ≈500 white dwarf stars as a part of this survey. After serendipitously finding two gas-disk-hosting white dwarf stars, we began routinely using a spectral setup that covered the Ca II infrared triplet (IRT) region where the strongest gas-disk emission lines are typically seen (e.g., Melis et al. 2010; Manser et al. 2016b, and references therein).

Table A1 lists all observation dates and resulting data properties. Grating resolution optical spectroscopy was performed at Lick Observatory with the Kast Double Spectrograph mounted on the Shane 3 m telescope and at Gemini-South with GMOS (Hook et al. 2004; hereafter GMOS-S). In general, all Kast observations employed the blue and red arms with light split by the d57 dichroic around 5700 Å. After splitting, blue light was passed through the 600/ 4310 grism, while red light was in most observations passed through the 830/8460 grating (and in a few, the 600/7500grating, which provided broader wavelength coverage). Slit widths of 1", 1."5, and 2" were used depending on seeing and cloud extinction; integration times ranged between 30 and 60 minutes depending on target brightness and conditions. GMOS-S observations used the B600 grating and a slit size of 0"5, were centered at a wavelength of 525 nm, and exposed for 15–20 minutes. GMOS-S spectra are recorded onto three detectors with a gap in wavelength coverage between each detector; we did not use multiple setups to cover these gaps. Final GMOS-S wavelength coverage is given in Table A1. Grating resolution data are reduced using standard IRAF longslit tasks including bias subtraction, flat-fielding, wavelength calibration with arc lamps, and instrumental response calibration via observations of flux calibration standard stars. Arc lamp frames are not obtained close in time to science frames and as such the zero-point of the wavelength scale is not accurate.

Higher-resolution observations were obtained for new gasdisk white dwarf systems with the Keck I telescope and HIRES at Maunakea Observatory (Vogt et al. 1994) and with the Baade telescope and MagE at Las Campanas Observatory (Marshall et al. 2008). HIRES data were taken with the C5 decker (1.148 slit width), had exposure times of 30–80 minutes, and were reduced using the MAKEE software package that outputs heliocentric velocity-corrected spectra shifted to vacuum wavelengths. While HIRES wavelength coverage is quoted as continuous in Table A1, there are gaps in coverage between each of the three CCDs and sometimes between red orders. MagE data were taken with the 0.15 slit, integrated for 60 minutes, and were reduced with the facility Carnegie Python pipeline (Kelson et al. 2000; Kelson 2003). After reduction and extraction, polynomials are fit to each order to bring overlapping order segments into agreement before combining all orders of every exposure to generate a final spectrum for analysis. More details about reducing echelle data in the presence of gas-disk emission lines can be found in Melis et al. (2010).

3. Measurements

3.1. Atmospheric Parameters and Abundances

For each target we use low-resolution data to obtain atmospheric parameters (e.g., $T_{\rm eff}$, $\log g$) and then measure abundances for any detected metallic absorption lines. In this paper we only report on elements detected in the low-resolution spectra; results from higher-resolution spectra will appear in future publications dedicated to atmospheric pollution. Fitting proceeds as in Melis et al. (2011), Melis & Dufour (2017), and references therein. We briefly summarize this process here.

To obtain atmospheric parameters we perform model fits to hydrogen Balmer lines and helium lines in the low-resolution data. The method follows the "spectroscopic technique" described by Bergeron et al. (1992) and described at length in Liebert et al. (2005) and references therein. Gaia DR2 distances are used to help constrain the stellar radius and hence $\log g$. Uncertainties for resulting $T_{\rm eff}$ and $\log g$ values are not calculated individually for each star, but are typically $\pm 1000~{\rm K}$ for $T_{\rm eff}$ and $\pm 0.1~{\rm dex}$ for $\log g$ (e.g., Bergeron et al. 2019; Genest-Beaulieu & Bergeron 2019a, 2019b, and references therein).

When metallic absorption lines are present in the lowresolution spectra, we measure abundances by fitting synthetic model spectra to the data. A grid of local thermodynamic equilibrium model atmospheres are generated with code similar to that described in Dufour et al. (2005, 2007) where absorption line data are taken from the Vienna Atomic Line Database. Synthetic spectra in the grid cover a range of abundances typically from $\log[n(Z)/n(H \text{ or He})] = -3.0 \text{ to } -8.0 \text{ in steps}$ of 0.5 dex. We then determine the abundance of each element by fitting the various observed lines using a similar method to that described in Dufour et al. (2005). This is done by minimizing the value of χ^2 taken as the sum over all frequencies of the difference between the normalized observed and model fluxes (the synthetic spectra are multiplied by a constant factor to account for the solid angle, and the slopes of the spectra locally are allowed to vary by a first-order polynomial to account for residuals from the spectral normalization procedure), all frequency points being given an equal weight. Interpolation between grid points allows us to achieve individual line abundances accurate to <0.05 dex. Uncertainties are conservatively set at 0.2 dex.

Table 1 reports modeled $T_{\rm eff}$, log g, and abundances for Ca and/or Mg (the most readily detectable elements in low-resolution optical spectra); corresponding white dwarf masses and radii are obtained from the MWDD⁶ evolutionary models (Bédard et al. 2020). For the two helium-dominated atmosphere stars we also report measured hydrogen abundances in their atmospheres. For Gaia J0611–6931 we report on the additional detection of Si in Section 4.5.

http://dev.montrealwhitedwarfdatabase.org/evolution.html

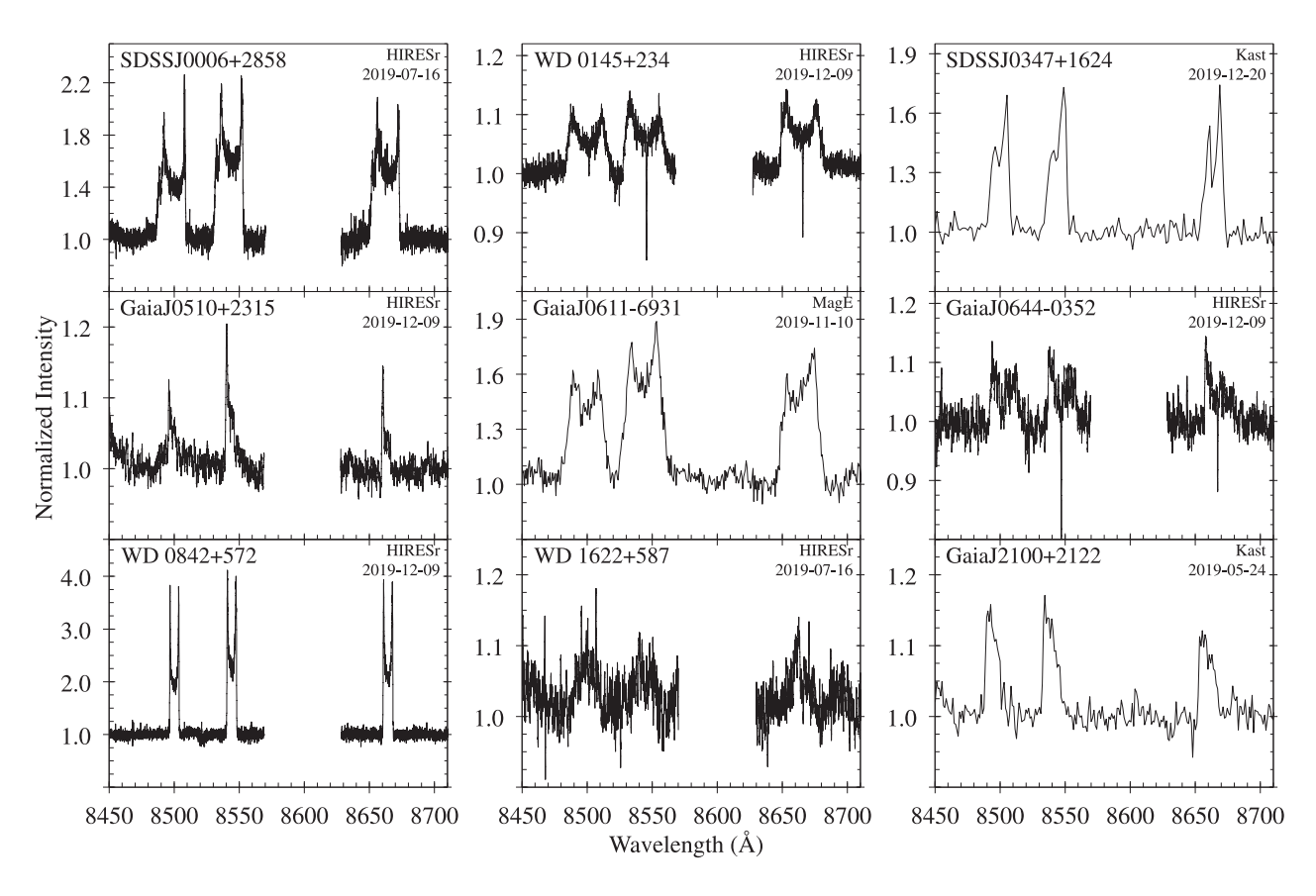


Figure 1. An individual epoch of Ca II IRT emission for each of the nine white dwarfs discovered in this work to host a gas disk. In all cases, spectra are continuum normalized. Wavelengths for HIRES data are in vacuum and shifted to the heliocentric reference frame. Kast spectra have wavelengths presented in air and are not shifted to the heliocentric reference frame. In some cases the HIRES spectra are smoothed with a 5 or 11 pixel boxcar for display purposes. More complete spectra and multiple epochs for each star are presented in Appendix B.

Table 1
White Dwarf Parameters

Object	R.A. (J2	Decl. 000)	$G_{ m mag}$ (mag)	Primary Atm. Const.	T _{eff} (K)	log g (cgs)	Mass (M_{\odot})	Radius (R_{\odot})	[Ca/H(e)] (log abund	[Mg/H(e)] dance by #)
SDSS J0006+2858	00 06 34.713	+28 58 46.54	16.37	Н	26,000	8.0	0.64	0.013	_	_
WD0145+234	01 47 54.818	$+23\ 39\ 43.60$	14.05	Н	12,720	8.1	0.67	0.012	-6.6	-5.9
SDSS J0347+1624	03 47 36.692	+16 24 09.73	16.65	Н	21,815	8.1	0.69	0.012	_	_
Gaia J0510+2315	05 10 02.146	+23 15 41.42	15.06	Н	21,700	8.2	0.75	0.011	_	-5.5
Gaia J0611-6931	06 11 31.699	$-69\ 31\ 02.15$	16.80	Н	17,900	8.2	0.74	0.011	-6.2	-4.6
Gaia J0644-0352	06 44 05.231	$-03\ 52\ 06.42$	16.19	He ^a	18,350	8.2	0.72	0.011	-6.7	_
WD0842+572	08 46 02.473	+57 03 28.64	16.81	Н	16,225	8.0	0.62	0.013	_	-3.9
WD1622+587	16 22 59.645	+58 40 30.89	16.87	He ^a	18,850	7.8	0.49	0.015	_	_
Gaia J2100+2122	21 00 34.648	+21 22 56.89	15.19	Н	26,550	8.1	0.70	0.012	_	-5.0

Notes. Abundances are quoted relative to the primary atmospheric constituent, hydrogen (H) or helium (He). The primary atmospheric constituent is indicated in the "Primary Atm. Const." column. A "—" in the abundance column means no metal absorption lines are seen in the Kast spectra.

3.2. Gaseous Emission Lines

Broad emission lines from several atomic transitions are detected in our optical spectra. Figure 1 shows Ca II IRT emission from one epoch for each source, while Figures B1–B33 show most other emission lines detected for each source and compare multiple epochs when such data are available. In many cases identifications for emission lines seen could be taken from past studies of white

dwarfs with gaseous disks (e.g., Gänsicke et al. 2006; Manser et al. 2016b, and references therein). In some cases lines seen did not have corresponding identifications in the literature and we sought to identify them. The procedure used for obtaining and assessing new line identifications is given below after discussion regarding basic measurements we make for each line.

For each feature we make several measurements. First is the emission line equivalent width that is uncorrected for line

^a Hydrogen is also detected in the atmospheres of Gaia J0644–0352 and WD1622+587; we obtain $log_{10}(H/He) = -5.1$ and $log_{10}(H/He) = -4.8$ respectively.

absorption in the feature. From this value, one may calculate a line flux; we do not do that here. Equivalent width uncertainties are obtained by taking the standard deviation of several measurements that differ by anchoring the continuum points for the measurement at multiple locations consistent within the spectrum noise level.

Next, we measure maximum gas velocities in the blue and red wings of the detected emission line and/or the full velocity width of a feature at zero intensity (effectively red-blue extent). The highest-velocity gas emission (reported as $v_{\text{max}} \sin i$) corresponds to the innermost orbit of emitting gasphase metals around each white dwarf (e.g., Horne & Marsh 1986). This value is quoted as a product with $\sin i$ where i is the unknown inclination angle of the disk (i of 0° would be obtained for a face-on disk). Maximum gas velocities are calculated relative to the white dwarf systemic motion. To derive each object's systemic motion, we measure radial velocities for metal and hydrogen lines in high-resolution spectra and then correct them for the computed gravitational redshifts at the white dwarf photosphere. Gravitational redshifts are based on measured atmospheric parameters reported in Table 1 and have uncertainties of up to $\sim 15 \,\mathrm{km \, s^{-1}}$ due to uncertainties in atmospheric parameter determinations; we do not include this additional error term in any analysis. Systemic velocities are reported in Table A2 along with other astrometric and kinematic quantities for each star.

Last, if possible, we measure the velocity separation between peaks for double-peaked profiles. Peak separation gives a rough characterization of the outermost orbit of emitting gas-phase metals and is obtained by taking the difference of each transition's peak centroid wavelengths. These are measured by making several Gaussian fits to each peak, changing between each fit the anchor points; the average is the adopted value and standard deviation the uncertainty.

Measurements are only made for lines with sufficiently good signal to noise such that both peaks are well detected and/or where one can clearly identify the line edges (where the line emission reaches zero intensity and the continuum emission level is recovered). In lower-resolution data, where the absolute wavelength scale is not accurate, we do not report maximum gas velocities relative to the white dwarf systemic motion. Full widths can be measured in all spectra as those are derived from the difference between blue and red extents of a line and are not affected by absolute wavelength scale inaccuracies. When there is the possibility of contamination by nearby transitions (whether in emission or absorption) we do not make measurements. For example, we typically cannot make measurements for the Fe I λ 5169 and Mg I triplet features around 5170 Å (e.g., see Figure B24).

For new and unidentified lines we follow a two-step, iterative process in establishing and assessing line identifications; this procedure relies upon high-resolution data and thus was not attempted with Kast or GMOS-S spectra. We begin with the selection of lines whose identifications we believe are unambiguous (e.g., Ca II IRT, O I, select Fe II, and Ca II H+K lines). From this selection of lines we establish a range of transition characteristics (lower and upper energy levels, Einstein coefficients, and oscillator strengths) and measured line extents in the red and blue wings ($v_{\rm max} \sin i$). We then search near the wavelength of an unidentified line for any transition with comparable transition characteristics to the known lines that also produces $v_{\rm max} \sin i$ values reasonably in

agreement with those seen for that target star. We used the NIST Atomic Spectra Database Lines Form⁷ and the database of van Hoof (2018)⁸ to obtain line parameters. With "candidate" line identifications obtained in this manner, we then perform a self-consistency check of seeking out other lines from the same element and ionization state that we might expect to see based on energy levels, transition probabilities, and oscillator strengths. Confirmation of such lines solidifies a line identification.

We have newly identified several Fe I (including some semi-forbidden) and Fe II lines, a semi-forbidden Ca I line, a Si I line, a semi-forbidden Mg I line, and Na D doublet emission. Ambiguous and unidentified lines remain; many likely originate from iron but it is not clear which specific transition is responsible. There are lines for which identifications are not possible because they were covered only with low-resolution spectra (see Section 4.4).

Table 2 reports all transitions detected for each source in any given epoch. Measured values for lines are reported in Tables B1–B9.

4. Individual Systems

Here we briefly discuss results for each target, including any literature work that may exist for each system.

4.1. SDSS J0006+2858

SDSS J0006+2858 was one of two stars (the other being Gaia J2100+2122) serendipitously found to host unambiguous emission lines early in our Kast polluted white dwarf survey and prompted a shift in our observing strategy to cover Ca II IRT lines.

SDSS J0006+2858 hosts a rich emission spectrum with lines from oxygen, calcium, and iron seen (Figures B1–B4). Emission structures in the 6200–6500 Å region similar to those seen in the spectrum of Gaia J0510+2315 are seen (Section 4.4); it is not clear what transitions they originate from. Possible contributions from magnesium may also be present near 5170 Å, but are inconclusive due to the presence of strong Fe II λ 5169 and λ 5197 emission. SDSS J0006+2858 hosts Ca II IRT line strengths comparable to some of the strongest known emitters (e.g., SDSS J1228+1040 and Gaia J0611-6931). Curiously, it also appears to host a third peak in its IRT lines that falls on the blue shoulder of the blueward major peak. Such a structure has not been previously seen for any other gas-disk white dwarf star.

Of special note for this system is a significant asymmetry in the maximum blue and red velocities of its emission lines. On average, the blue line extent is roughly double that seen in the red ($-800~{\rm km\,s}^{-1}$ versus $+400~{\rm km\,s}^{-1}$; see Table B1 and Figure 2). Uncertainties in stellar atmospheric parameters (and hence gravitational redshift) combined with line measurement uncertainties are not capable of accounting for this difference. While this asymmetry is seen in all lines, the strength of the "extended" portion in the blue wing is suppressed in the Ca II IRT relative to what is seen for other transitions (including Ca II H+K). This extension in the blue wing is stable over at least a 1 week timescale (2019 July 7 and 16

https://physics.nist.gov/PhysRefData/ASD/lines_form.html

⁸ http://www.pa.uky.edu/~peter/newpage/

Table 2
Observed Emission Lines

					erved Emission					
Element	Rest $\lambda_{\rm air}$	SDSS J0006	WD0145	SDSS J0347	Gaia J0510	Gaia J0611	Gaia J0644	WD0842	WD1622	Gaia J2100
Oxygen										
OI	7772	Y	_	W	Y	W	_	_	Y	W
O I	8446	W	_	_	W	W	_	_	_	w
Sodium										
Na I	5890	_	_	_	_	Y	_	_	_	_
Magnesiun										
Mg I]	4571.095	_	_	_	_	_	_	Y	_	_
Mg I	5167.321	?	_	?	?	Y	_	Y	?	_
Mg I	5172.684	?	_	?	?	Y	_	Y	?	_
Mg I	5183.604	?	_	?	W	Y	_	Y	?	_
Mg I	8806.76	?	?	_	?	Y	?	?	?	?
Mg II	7877.05	_	_	_	W	_	_	_	_	_
Mg II	7896.37	_	_	_	W	_	_	_	_	_
Silicon										
Si I	3905.523	_	_	_	_	Y	_	w	_	_
Calcium										
Ca I]	6572.78	_	_	_	_	_	_	w	_	_
Ca II	3933.663	w	_	_	_	Y	_	w	_	_
Ca II	3968.469	W	_	_	_	W	_	w	_	_
Ca II	8498.023	Y	Y	Y	W	Y	Y	Y	w	Y
Ca II	8542.091	Y	Y	Y	Y	Y	Y	Y	w	Y
Ca II	8662.141	Y	Y	Y	W	Y	Y	Y	w	Y
Neutral Iro	n									
Fe I]	4375.929	_	_	_	_	_	_	Y	_	_
Fe I]	4427.310	_	_	_	_	_	_	Y	_	_
Fe I]	4461.652	_	_	_	_	_	_	w	_	_
Fe I	5012.068	?	_	?	_	_	?	Y	?	?
Fe I]	5110.413	_	_	_	_	_	_	Y	_	_
Ionized Iro	on									
Fe II	4178.853	w	_	_	_	_	_	w	_	w
Fe II	4233.162	w	_	_	_	_	_	w	_	w
Fe II	4351.762	w	_	_	_	_	_	w	_	w
Fe II	4416.818	w	_	_	_	_	_	_	_	w
Fe II	4515.333	w	_	_	_	_	_	w	_	w
Fe II	4520.218	w	_	_	_	_	_	_	_	w
Fe II	4522.627	w	_	_	_	_	_	_	_	w
Fe II	4549.466	w	_	w	_	_	_	w	_	w
Fe II	4583.829	w	_	w	w	_	_	w	_	Y
Fe II	4629.332	w	_	w	w	_	_	w	_	Y
Fe II	4923.921	Y	_	w	Y	_	?	Y	?	w
Fe II	5018.436	Y	_	Y	Y	_	?	Y	?	Y
Fe II	5169.028	Y	_	Y	Y	?	_	Y	?	Y
Fe II	5197.57	w	_	w	w	?	_	_	_	w
Fe II	5234.62	w	_	w	w	_	_	w	_	w
Fe II	5276.00	w	_	w	w	_	_	w	w	w
Fe II	5316.609	Y	_	Y	Y	_	_	Y	w	Y
Fe II	6458.164	w	_	W	w	_	_	w	_	w
Fe II	7711.720	_	_	w	w	_	_	w	_	w
	s or Unidentifi	ed								
?	4202	w	_	_	_	_	_	_	_	W
?	4488	_	_	_	w	_	_	W	_	-
Fe I?	5052	w	_	_	- -	_	_	W	_	_
?	6160	_	_	_	_	w	_	_	_	_
?	6240	w	_	w	w	w	_	_	_	_
?	6318	w ?	_	w	w W	vv	_		_	_
?	6347	<i>:</i> —	_	w _	W W	_	_	_	_	_
?	6382		_			_	_	_	_	
?		W	_	W	W	_				W
	6515 7506	w _	_	w _	W W	_	_	Y -	_	W
?										

Note. For each star and transition, a "-" means no line was seen in any epoch, "w" means a weak transition is seen, "Y" means a clear emission line is seen, and "?" means this wavelength was not covered by our observations or lies within a strong transition that prevents conclusive analysis. SDSS J0347+1624 was only observed with the Kast; all other stars have higher-resolution data products.

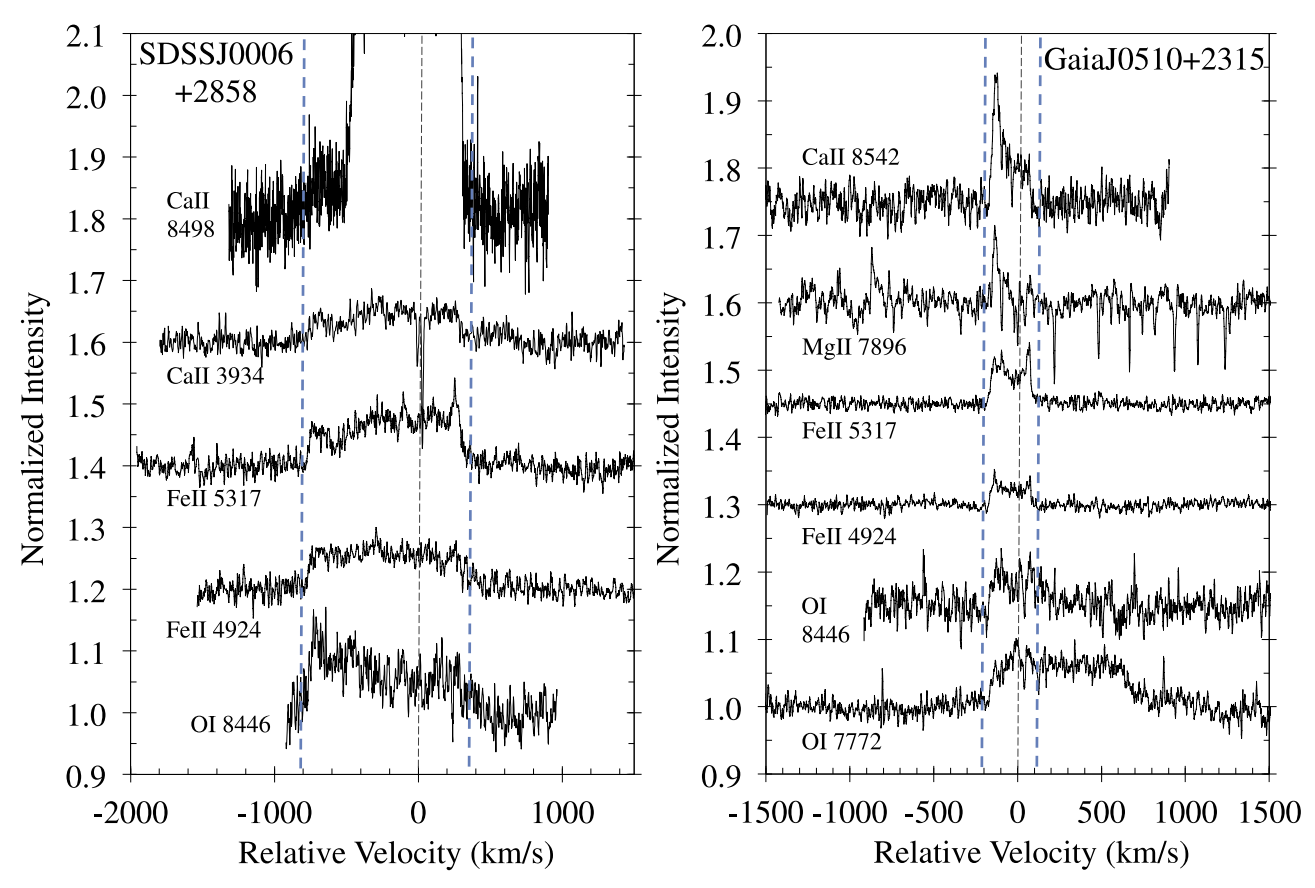


Figure 2. Velocity-space plots with representative emission lines for each element detected for SDSS J0006+2858 (left) and Gaia J0510+2315 (right). Continuum levels have been fit and divided into each HIRES spectral segment shown and individual segments offset by an additive constant for purposes of clarity. A velocity of 0 corresponds to the calculated systemic velocity for each star (Section 3.2 and Table A2). Blue vertical dashed lines give the measured average maximum gas velocities seen in the blue and red wings of emission lines (Section 3.2 and Tables B1 and B4). Clear velocity asymmetry is seen in the red and blue wings of all elements for SDSS J0006+2858, while more subtle velocity asymmetry is seen for Gaia J0510+2315. Extended red wing emission in the O1 λ 8446 complex for SDSS J0006+2858 is due to a blend of multiple lines; the range delineated by the vertical dashed lines is centered on the lowest wavelength transition in the multiplet. For Gaia J0510+2315, O1 lines near 7772 and 8446 Å are significantly more extended than other emission lines (see Section 4.4).

HIRES measurements) and possibly over 6 month timescales (Figures B1 and B4).

4.2. WD0145+234

WD0145+234 was first reported as a spectroscopically confirmed white dwarf star with spectral type DA by McCook & Sion (1987). It was further studied in Gianninas et al. (2011) and Limoges et al. (2015) where they measured from spectroscopic observations a DA spectral type, an effective temperature of $\approx 13,000 \pm 200$ K, and $\log g$ of $\approx 8.12 \pm 0.05$. Gianninas et al. (2006) performed high-speed optical photometric monitoring of WD0145+234 over a couple hours in one night, finding no obvious variability over period ranges of 20–2000 s with a detection limit of 0.06%; they also derived from spectra $T_{\rm eff} = 12,470$ K and $\log g$ of 8.06. Similar results in optical monitoring were found in the study performed by Bognár et al. (2018). Rebassa-Mansergas et al. (2019) identify WD0145+234 as an infrared excess candidate and associate its excess emission to a putative debris disk.

More remarkably, WD0145+234 was recently reported in the literature to have undergone an outburst in the mid-infrared (Wang et al. 2019). Pre-outburst archival observations demonstrate that it was host to atmospheric pollution (but past studies of this star did not note atmospheric pollution) and infrared excess emission indicating that the white dwarf star is

in the process of consuming a rocky body from its remnant planetary system (Wang et al. 2019; Melis et al. 2021, in preparation). The infrared excess emission is now brighter by over a magnitude, likely due to a fresh disintegration event off of a rocky body.

The infrared outburst at WD0145+234 began in mid-2018 (Wang et al. 2019); the observations of gas emission were in late 2019 (Table A1). Since no strong emission lines other than the Ca II IRT are seen (Table B2 and Figure B5), and since no archival observations covering the Ca II IRT exist that we are aware of, it is not possible to comment on whether or not gaseous emission lines were present in spectra taken before the infrared outburst began. No obvious variability is seen in the gas emission lines (strength or structure) between the epochs presented here (Table B2 and Figure B5).

An exhaustive study on the time variability of absorption lines and the composition of the parent body source of the material being accreted by WD0145+234 will appear elsewhere (Melis et al. 2021, in preparation).

4.3. SDSS J0347+1624

SDSS J0347+1624 was brought to our attention by Dennihy et al. (2020) as a new gas-disk candidate. We had obtained observations of it in 2016 and obtained a further spectrum in 2019 to aid in the variability study being conducted by

Dennihy et al. We present the Kast spectra obtained in both epochs here, but defer to Dennihy et al. (2020) for a full discussion of this source.

Kast spectra from both epochs show clear emission from oxygen, calcium, and many iron lines (Figures 1 and B6–B8); unidentified emission in the 6200–6500 Å region similar to that seen for Gaia J0510+2315 may also be present (Section 4.4). The Kast data do not reveal any detectable variation between iron lines in the 2016 and 2019 epochs (2016 epoch spectra did not cover beyond 7700 Å and hence only covered iron emission line regions in common with the 2019 epoch; Tables A1 and B3).

4.4. Gaia J0510+2315

Emission lines from oxygen, magnesium, calcium, and iron are seen toward Gaia J0510+2315 (Figures B9-B14). Gaia J0510+2315 is the only star in the sample to host clear emission from Mg II, in this case near 7900 Å (Figure B13). It is also impressive in that both O I emission features are comparable in strength to the Ca II IRT emission lines (Table B4 and Figures B13 and B14).

No obvious variability is seen between epochs. Two emission structures that we cannot identify appear in Kast data at wavelengths that are not covered by the HIRES spectra (Table 2 and Figures B9 and B13). Emission in the 6200–6500 Å region, likely from iron, is seen in Kast and HIRES spectra (Figure B12).

Apparent asymmetry is seen in the blue and red wings of emission lines when one considers all maximum velocity measurements together (Figure 2 and Table B4). Curiously, and unique to Gaia J0510+2315, the O I triplet near 7772 Å (and possibly the O I complex near 8446 Å) hosts a red extent that greatly exceeds measurements for any other line (Table B4 and Figures 2 and B13). It is not clear if some blended emission lines are responsible for this or if the distribution of oxygen gas near Gaia J0510+2315 is different from other elements (in this case extending much closer to the star).

4.5. Gaia J0611-6931

GMOS-S and MagE spectra indicate that Gaia J0611-6931 hosts strong atmospheric metal pollution and hitherto unseen emission from the Na D doublet (Figure B17). Also anomalous was the identification of Si I $\lambda 3905$ emission that is otherwise only seen in WD0842+572 (Table 2). Gaia J0611-6931 otherwise hosts familiar transitions from oxygen, magnesium, calcium, and iron (Figures B15-B19).

No variability is seen between emission lines in the GMOSS and MagE epochs (Table B5). Possible emission is seen in a variety of places in the spectra, but is hard to confirm due to signal-to-noise constraints and systematics present in the data including fringing. Weak emission may be present near the core of the H δ photospheric absorption line, a feature we cannot verify nor identify with the data in hand (Figure B15; it is possible that similar emission may also be present for SDSS J0006+2858 and Gaia J2100+2122). The appearance of the line in the core of H δ is reminiscent of what is seen in the core of the He I λ 5876 line for helium-dominated atmosphere white dwarfs (Klein et al. 2020), but without similar cores in other Balmer transitions the feature is probably not due to hydrogen. In general there appear to be multiple emission complexes between 6100 and 6300 Å (Figure B17), but it is not

clear if the emission is real and similar to what is seen in this region for other stars (Table 2 and Figure B12).

Beyond the unusual volatile emission from sodium, Gaia J0611-6931 also stands out as having some of the strongest Ca II IRT emission lines seen in any gas-disk star (Table B5) and the second-highest magnesium abundance in the sample presented herein (Table 1). Additionally, we see even in low-resolution spectra photospheric absorption lines from Si II near 6350 and 6370 Å (Figure B17). We fit these lines in addition to Ca II and Mg II absorption lines finding a silicon abundance by number of $log_{10}(Si/H) = -4.8$ (these values also provide a reasonable fit to the higher-resolution MagE detections of these lines). Limits for iron and oxygen are not restrictive (oxygen especially being confounded by emission), so it is not possible to comment further on the composition of the parent body polluting Gaia J0611-6931. While it may be tempting to credit the presence of volatile emission seen for Gaia J0611-6931 to a volatile-rich nature of the parent body it is accreting, it is prudent to wait for complete disk and/or atmospheric abundances before arriving at such a conclusion (e.g., see the cautionary tale for overinterpreting gas emission strength as abundance in Matlovič et al. 2020).

4.6. Gaia J0644-0352

Only weak Ca II IRT emission lines are seen in HIRES data for this star (Figure 1). There may also possibly be a very weak hint of emission from Fe II $\lambda 5316$, but with no other iron lines detected this is considered inconclusive. While the measurements have fairly high uncertainty (due to the low significance of the line detections), there could be a slight hint of asymmetry in the maximum blue and red velocity gas seen (Table B6).

Gaia J0644–0352 is notable for being one of two helium-dominated atmosphere stars in the sample. The star also has hydrogen detected in low-resolution spectra indicating the possibility of a parent body having some amount of water (e.g., Gentile Fusillo et al. 2017). A complete atmospheric abundance and oxygen budget analysis (e.g., Klein et al. 2010; Farihi et al. 2013) will be necessary to determine how much water the parent body contained.

4.7. WD0842+572

Initial detection and spectroscopy for WD0842+572 was conducted as a part of the Second Byurakan Sky Survey where the star was found to have a spectral type of DA (Balayan 1997a). Until recently this star was not prominently featured in any published work. In Swan et al. (2020), Spitzer warm IRAC photometry is presented along with a private communication noting that the star is host to gas-disk emission lines.

WD0842+572 is host to a selection of narrow emission lines with typically well-defined double-peak morphology. We find contributions from silicon, magnesium, calcium, and iron (Figures B20–B26).

Several characteristics make WD0842+572 stand out compared to the rest of the sample. First is the highest atmospheric abundance of magnesium for any star in our sample (Table 1). Second is the clear detection of a semi-forbidden transition of magnesium, Mg I] λ 4571 (Figure B22), and a bevy of semi-forbidden neutral iron lines between 4300 and 5200 Å (Figures B21 and B23). Additionally, semi-forbidden neutral calcium is seen in the red wing of the H α photospheric

absorption line (Figure B25). Last is a preponderance of emission lines from neutral atomic species like Mg I, Si I, Ca I, and Fe I (Figures B20–B25). Notably absent is emission from the O I triplet near 7772 Å, which is seen at most other systems presented herein.

Strong Ca II IRT lines are seen for this star (Figure B26), but do not quite rise to the level of the strongest emitters known (Table B7). Possible variation is hinted at in the structure of lines seen between the Kast and HIRES epochs (separated by roughly 6 months). Whether this variation is due to the lower resolution in the Kast data or true changes in the lines is not clear from the data available; in any case, Kast line measurements differ from what is measured with HIRES at the $\lesssim 3\sigma$ level (see Table B7).

4.8. WD1622+587

Spectroscopic characterization of WD1622+587 was performed through the Second Byurakan Sky Survey where it was found to have a spectral type of DB (Balayan 1997b). The star received little attention following that initial observation and until now was not singled out individually in any published study.

Oxygen, calcium, and iron emission lines are seen in WD1622+587 (Figures B27–B29). Most lines are only seen in the HIRES data, although slight hints of Ca II IRT emission are seen in Kast spectra (Figures B28 and B29); we do not attempt measurements for these low-significance lines. Oxygen emission in the 7772 Å complex is comparable in strength to the individual Ca II IRT lines (Table B8), although no oxygen emission from the 8446 Å complex is seen.

WD1622+587 is a helium-dominated atmosphere star, also with hydrogen present, similar to Gaia J0644-0352 (Table 1).

4.9. Gaia J2100+2122

Gaia J2100+2122 has an emission spectrum dominated by iron lines, a feature that made it a clear emission line star despite discovery Kast spectra not covering Ca II IRT lines (Figures B30 and B31). Emission is also seen from oxygen and calcium (Figures B32 and B33). Gaia J2100+2112 also hosts unidentified emission in the 6200-6500 Å region like in the spectrum of Gaia J0510+2315 (Figure B12).

While most iron and oxygen lines are relatively similar between epochs, variability is present at the $\gtrsim 3\sigma$ level for Ca II IRT lines between the HIRES and Kast epochs (Table B9 and Figure B33). Gaia J2100+2122 thus stands out as the only star for which we saw variability beyond measurement uncertainties. Dennihy et al. (2020) showcase the variability for this source across several epochs.

5. Discussion and Conclusions

The nine stars presented herein significantly enlarge the known sample of single white dwarfs that host gaseous debris disks. Previously known in the literature were SDSS J0738 +1835 (Brinkworth et al. 2012; Dufour et al. 2012), Ton 345 = SDSS J0845+2257 (Gänsicke et al. 2008; Melis et al. 2010), WD J091405.30+191412.25 (Gänsicke et al. 2019), SDSS J0959-0200 (Farihi et al. 2012), SDSS J1043+0855 (Gänsicke et al. 2007; Melis et al. 2010; Manser et al. 2016a), SDSS J1228+1040 (Gänsicke et al. 2006; Melis et al. 2010; Hartmann et al. 2016; Manser et al. 2016b, 2019), HE 1349 -2305 (Melis et al. 2012; Dennihy et al. 2018), and

SDSS J1617+1620 (Brinkworth et al. 2012; Wilson et al. 2014). Two sources claimed in the literature to be single white dwarfs hosting gas disks have been refuted (SDSS J1144+0529 reported first by Guo et al. 2015 and refuted by Swan et al. 2020 and Florez & Wilson 2020, and SDSS J1344+0324 reported first by Li et al. 2017 and refuted in Xu et al. 2019). In sum, 17 gas-disk-hosting white dwarfs are now known.

As an ensemble, the known gas-disk-hosting white dwarf stars have an average effective temperature of $\approx\!18,\!500\,\mathrm{K}$ with a standard deviation of $\pm 4500\,\mathrm{K}$. There are four sources in the sample with effective temperatures $\leqslant 1$ standard deviation from the mean: SDSS J0738+1835 ($T_{\rm eff}\approx 14,\!000\,\mathrm{K}$; Dufour et al. 2012), SDSS J1617+1620 ($T_{\rm eff}\approx 13,\!500\,\mathrm{K}$; Brinkworth et al. 2012), SDSS J0959-0200 ($T_{\rm eff}\approx 13,\!300\,\mathrm{K}$; Farihi et al. 2012), and WD0145+234 ($T_{\rm eff}\approx 12,\!720\,\mathrm{K}$; Table 1). SDSS J0959-0200 and SDSS J1617+1620 are known to host highly variable IRT emission line strengths. On intra-night to $\sim\!\!$ few month temporal baselines WD0145+234 shows no evidence for variability (Figure B5).

WD0145+234 narrowly finds itself as the new "coolest" gas-disk-hosting white dwarf known; it is not clear what role (if any) the recent infrared "outburst" may have had in producing the detected gas disk. All of the cool gas-disk stars named in the previous paragraph have so far been found to host only Ca II IRT emission lines. An examination of summed Ca II IRT emission line equivalent width as a function of host white dwarf $T_{\rm eff}$ reveals considerable scatter at all effective temperatures. However, there appears to be an upper envelope of maximum observed Ca II IRT equivalent widths of $\approx 50 \text{ A}$ for hotter white dwarfs that is significantly lower (\approx 10–20 Å) for white dwarfs with $T_{\rm eff}$ < 16,000 K. With only four sources known to date in this temperature range it is not clear if this is the result of observational bias or actual physical processes at play (e.g., disk heating from energetic photons as described in Melis et al. 2010).

Three-dimensional Galactic UVW space motions are computed and presented for all systems discovered through this work (Table A2). Additionally, space motions were adopted for Ton 345, SDSS J1043+0855, and SDSS J1228+1040 from Melis et al. (2010). Kinematic measurements for HE 1349 -2305 from Melis et al. (2012) are used to calculate *UVW*: $U = +3 \text{ km s}^{-1}$, $V = -11 \text{ km s}^{-1}$, and $W = -4 \text{ km s}^{-1}$. As a whole for the class of gas-disk single white dwarf stars, we see consistently negative Galactic V velocities, similar to V velocities for white dwarfs with and without atmospheric pollution (see Table 6 of Zuckerman et al. 2003; Table 4 of Zuckerman et al. 2010). As such, gas-disk-hosting white dwarfs do not appear to be kinematically "special" compared to other white dwarf stars and join them in having space motions characteristic of an old population trailing the local standard of rest as they orbit around the Galactic center.

Within the sample of new emission line stars presented herein we see a distribution of host star primary atmospheric types (hydrogen or DA, helium or DB) of $\approx 78\%$ DA and 22% DB. For the 17 total gas-disk-hosting systems now known, this distribution is 71% DA and 29% DB. Both are a reasonable match to what is observed in the field population of white dwarf stars (e.g., Kilic et al. 2020, and references therein). As such, it is safe to conclude there is no bias for gas disks to be present around DB or DA white dwarfs.

Previously identified gas-disk white dwarfs have, with the exception of SDSS J1228+1040 and WD J091405.30

+191412.25, typically only been seen to host emission from calcium and sometimes iron. SDSS J1228+1040 saw the additional identification of oxygen and magnesium (Manser et al. 2016b), while WD J091405.30+191412.25 hosts more unusual emission dominated by hydrogen, oxygen, and sulfur (the likes of which are due to accretion from a giant planet-like companion; Gänsicke et al. 2019). Two-thirds of the sample presented herein show at least oxygen, calcium, and iron, while a small subset additionally show magnesium and silicon (Table 2). Neutral silicon emission from the 3905 Å transition has never been documented before; we detect it unambiguously in the spectra of Gaia J0611-6931 and WD0842+572. Magnesium may be more prevalent than indicated by Table 2 as its neutral triplet transitions near 5170 Å are typically confused with iron emission in that region. The Mg I $\lambda 8806$ line appears to be comparably strong from Gaia J0611-6931 (Figure B19) and SDSS J1228+1040 (Manser et al. 2016b) and is not blended with other lines. Unfortunately, the HIRES red setup used for this study did not cover the 8806 Å region (it fell in an order gap). Gaia J0611-6931 is unique in the identification of sodium in its emission spectrum. The lack of hydrogen and other volatiles, combined with the detection of elements typically found in rocky minerals (both in emission and absorption), points to the gas originating in the destruction of rocky bodies. Future atmospheric pollution analyses and emission line modeling will reveal the elemental composition of the material producing the gas and being accreted by each host white dwarf.

As noted in Melis et al. (2010), emission line profiles observed at high spectral resolution exhibit a range of complex structures (e.g., Figure 1). It is tempting to attribute the range of observed line widths for gas-disk systems to different disk inclination angles. For example, WD0842+572 could be viewed nearly face-on while SDSS J0006+2858 could be viewed closer to edge-on (Tables B7 and B1). However, without performing detailed physical modeling for the gas and/ or dust disks in these systems, it is not possible to conclusively assign viewing geometries and thus arrive at gas-disk parameters like inner and outer radii (e.g., as in Melis et al. 2010). Emission line modeling that reproduces the observed line intensities and shapes will be necessary to arrive at robust gas-disk physical parameters (e.g., Gänsicke et al. 2019). Despite this, a speculative interpretation for the unusual characteristics seen in WD0842+572 is worth mentioning. The combination of its narrow line profiles, abundance of neutral emission line species, and presence of several semiforbidden transitions could be seen as evidence for a face-on viewing angle. The nearly zero sin i reduces the maximum velocity emission seen to its small (relative to other gas-disk systems) value, while the presence of neutrals and semiforbidden emission lines comes from primarily seeing the lower-density region of an optically thick disk's upper atmosphere.

Variability in gas-disk emission lines has been noted for several systems in the literature. Manser et al. (2016b) thoroughly characterize long-term changes in Ca II IRT emission features for SDSS J1228+1040, deciphering with Doppler imaging what appears to be a precessing eccentric gas ring (see more below). In a follow-up study dedicated to shorter timescales, Manser et al. (2019) find repeating changes with a period of ~2 hr in the Ca II IRT line strengths, which they interpret as evidence for an orbiting dense planetesimal.

Manser et al. (2016a) document variability over long timescales for SDSS J1043+0855. Wilson et al. (2014) demonstrate that SDSS J1617+1620 is highly variable, with Ca II IRT emission lines strengthening dramatically between 2006 and 2008, then monotonically declining thereafter. Dennihy et al. (2018) conducted a monitoring campaign for HE1349-2305, finding a cycling through having a red-dominated peak structure as found in Melis et al. (2012) to a blue-dominated peak structure and back to red-dominated again; a period of 1.4 yr is estimated. Wilson et al. (2015) and Manser et al. (2016a) show variability in line profiles for Ton 345.

The above, typically more exhaustive, studies showcase a wide range of variability behaviors for gas-disk emission systems. Variability in Gaia J2100+2122 (Table B9 and Section 4.9) and possibly in WD0842+572 (Table B7 and Section 4.7) are presented herein while Dennihy et al. (2020) showcase more extensive observations of SDSS J0347+1624 and Gaia J2100+2122. An interesting tie-in to gas-disk line variability comes from the recent explosion in dust-disk variability studies. Xu & Jura (2014) showed that SDSS J0959-0200 experienced a dramatic drop in its infrared dust emission levels, while Farihi et al. (2018) found similar behavior combined with re-brightening episodes for GD 56 (a star that does not host a known gaseous debris disk component). Wang et al. (2019) documented the "outburst" captured by the WISE satellite for WD0145+234. Swan et al. (2019, 2020) provide a more systematic study of infrared variability in white dwarf disk systems (those with dust only and both dust and gas) finding that gas-disk-hosting systems as a class show more variability in their dust continuum emission than non-gas-disk-hosting stars. They interpret this finding within the context of circumstellar material having a range of collisional activities, gas-disk systems being the more collisionally active cousins of the dust-only systems.

Manser et al. (2016b) demonstrate how emission line structures can change with time, in their case through the long time baseline study of SDSS J1228+1040. Gänsicke et al. (2006) and Melis et al. (2010) find maximum gas velocities for SDSS J1228+1040 of \approx 560 km s⁻¹ with observations conducted between 2003 and 2008. However, Melis et al. (2010) find an asymmetry in their 2008 measurements with the maximum blue wing emission being at $-380 \,\mathrm{km \, s^{-1}}$ and maximum red wing emission at $+550 \,\mathrm{km \, s^{-1}}$. During monitoring between 2011 and 2015, Manser et al. (2016b) show that this can evolve into a maximum blue extent of $-390 \,\mathrm{km \, s^{-1}}$ and maximum red extent of $+780 \,\mathrm{km \, s^{-1}}$ (it is not clear if these are ever achieved at the same time). SDSS J0006+2858 simultaneously hosts a maximum blue extent for its gas emission of $-800 \,\mathrm{km \, s^{-1}}$ and maximum red extent of $+400 \,\mathrm{km \, s}^{-1}$ over the time observations were collected for it in this work (Figure 2 and Table B1). Similar to that found here for SDSS J0006+2858, elements other than calcium in the spectrum of SDSS J1228+1040 also show the same asymmetry indicating well-mixed atomic species (Manser et al. 2016b).

The only other system to show pronounced red/blue asymmetry similar to SDSS J0006+2858 and SDSS J1228 +1040 is HE1349-2305. This star had in 2011 red and blue extents similar to that measured for SDSS J0006+2858 here (Melis et al. 2012). Dennihy et al. (2018) do not measure maximum red and blue gas extents in their monitoring study of HE1349-2305. Beyond these stars, possible asymmetries in maximum gas velocities may also be seen in Gaia J0510+2315

(Table B4), SDSS J1043+0855 (Melis et al. 2010), and Gaia J0644-0352 (Table B6). Thus, 6 out of 17 total gasdisk systems show evidence for asymmetric line profiles. It is not clear at this time if all such systems cycle through phases of exhibiting these asymmetries or if an era of asymmetric line extents is part of an evolutionary sequence that ends in fully symmetric and stable gas emission lines.

Starting with the discovery of single white dwarf stars with gaseous debris disks, it was recognized that these systems are likely host to eccentric gas rings (Gänsicke et al. 2006, 2007, 2008; Melis et al. 2010). This interpretation continued with the addition of new data sets and systems (e.g., Wilson et al. 2015; Manser et al. 2016a, 2016b, 2019). Indeed, an eccentric gaseous ring component has also been inferred for the transiting planetesimal system WD1145+147 (Cauley et al. 2018; Fortin-Archambault et al. 2020). Asymmetric gas emission line structures bolster such interpretations (e.g., Miranda & Rafikov 2018). Disk evolutionary models suggest that eccentric debris systems may reflect an early evolutionary state and that the material will eventually settle into a more circularized orbit (e.g., Veras et al. 2014; Nixon et al. 2020).

In conclusion, we present a set of nine new gas-disk-hosting single white dwarf stars. Some properties of these systems are similar to previously discovered gas-disk systems, while some display new and exotic features. Of special note is that only four of the known gas-disk systems are found south of the celestial equator, and of those only two are below a decl. of -5° . This likely implies a significant number of southernhemisphere gas-disk-hosting white dwarf stars remain to be discovered (at least 10 to balance the current population).

C.M. and B.Z. acknowledge support from NSF grants SPG-1826583 and SPG-1826550. B.K. acknowledges support from the APS M. Hildred Blewett Fellowship. A.E.D. acknowledges support from the NASA Exoplanets program award number 80NSSC20K0270. We thank E. Dennihy for useful discussion. Research at Lick Observatory is partially supported by a generous gift from Google. Some of the data presented herein were obtained at the W.M. Keck Observatory, which is operated as a scientific partnership among the California Institute of Technology, the University of California and the National Aeronautics and Space Administration. The Observatory was made possible by the generous financial support of the W.M. Keck Foundation. We acknowledge that Keck Observatory rests on land that is important and significant to the Hawaiian Natives in many ways. Similarly, we acknowledge that Lick Observatory resides on land traditionally inhabited by the Muwekma Ohlone Tribe of Native Americans. This research has made use of NASA's Astrophysics Data System, the National Institute of Standards and Technology Atomic Spectra Database Lines Form, the SIMBAD database, and the VizieR service.

Facilities: Shane(Kast), Keck I(HIRES), Gemini-South (GMOS), Magellan(MagE).

Appendix A Observations Summary and Target Kinematics Tables

Table A1 presents all observation dates and resulting data properties for spectra used in this work. Table A2 presents astrometric and kinematic properties for the systems studied.

Table	A1
Observations	Summary

Observation Date (UT)	Instrument Used	Wavelength Range (Å)	Resolving Power	S/N	$\lambda \text{ of S/N}$ (Å)
SDSS J0006+2858					
2018 Dec 29	Kast	3450–5475	900	36	5100
		5600-7850	2300	28	7450
2019 Jan 25	Kast	3450-5475	1300	38	5100
		6520-8785	3500	37	7450
2019 Jul 7	HIRES	3139-5950	40,000	38	5100
2019 Jul 16	HIRES	4720-8995	40,000	32	7450
2019 Jul 26	Kast	3450-5480	1300	48	5100
		5580-7850	3500	29	7450
WD0145+234					
2018 Nov 14	Kast	3420–5480	1300	55	5100
		5710-7820	3500	30	7450
2019 Sep 21	HIRES	3130-5950	40,000	53	5100
2019 Oct 12	Kast	3450-5480	1300	173	5100
		6440-8790	3500	165	7450
2019 Nov 4	Kast	3450-5465	1300	215	5100
		6440-8790	3500	195	7450
2019 Nov 18	Kast	3450-5460	1300	250	5100
		6465-8795	3500	220	7450
2019 Dec 9	HIRES	4720-8995	40,000	85	7450
SDSS J0347+1624					
2016 Oct 21	Kast	3450–5430	1300	50	5100
		5580-7690	3500	30	7450
2019 Dec 20	Kast	3450-5450	700	57	5100

Table A1 (Continued)

Observation Date (UT)	Instrument Used	Wavelength Range (Å)	Resolving Power	S/N	$\lambda \text{ of S/N} $ (\mathring{A})
		5750-8900	1700	59	7450
Gaia J0510+2315					
2019 Mar 18	Kast	3465–5450	900	62	5100
		6470-8760	2300	47	7450
2019 Nov 16	Kast	3450–5450	700	97 86	5100
2019 Nov 17	Kast	6475–8760 3450–5400	1700 900	86 113	7450 5100
2017 1407 17	Kast	5590-7830	2300	91	7450
2019 Nov 18	Kast	3450–5450	1300	180	5100
		6480-8770	3500	145	7450
2019 Dec 9	HIRES	4720–8995	40,000	65	7450
Gaia J0611-6931					
2019 Oct 10	GMOS-S	3700-4690	1750	65	4500
		4730–5750	2200	73	5100
2010 N 10)	5800-6820	2500	60	6200
2019 Nov 10	MagE	3120–9800	7500	46	7450
Gaia J0644-0352					
2018 Dec 16	Kast	3450-5450	1300	40	5100
		5720–7820	3500	25	7450
2018 Dec 28	Kast	3450–5450	700	42	5100
2010 Mar 19	Kast	5620–7840 2450–5450	1700 900	30 9	7450 5100
2019 Mar 18	Nast	3450–5450 6420–8780	2300	3	7450
2019 Dec 9	HIRES	4720–8995	40,000	26	7450
WD0842+572					
2019 Mar 18	Kast	3450–5470	900	30	5100
		6440–8775	2300	20	7450
2019 Apr 24	Kast	3450-5440	900	59	5100
		6460-8720	2300	47	7450
2019 May 29	Kast	3480–5450	900	16	5100
		6470–8760	2300	21	7450
2019 Dec 9	HIRES	4265–8995	40,000	31	7450
2020 Jun 15	HIRES	3130–5950	40,000	11	5100
WD1622+587					
2019 Jan 25	Kast	3450–5455	700	38	5100
2019 Apr 24	Kast	5700–7810 3450–5450	1700 900	35 44	7450 5100
2019 Apr 24	Kast	6420-8720	2300	37	7450
2019 Jul 12	Kast	3460–5420	900	53	5100
		6470–8770	2300	49	7450
2019 Jul 16	HIRES	4720–8995	40,000	21	7450
Gaia J2100+2122					
2018 Dec 16	Kast	3450–5450	700	21	5100
		5720-7820	1700	12	7450
2018 Dec 28	Kast	3450–5470	700	79	5100
2010 5	••	5600–7830	1700	63	7450
2018 Dec 30	Kast	3460–5450	700	91	5100
2019 May 24	Kast	5650–7830 3460–5460	1700 900	68 139	7450 5100
2017 Widy 24	KdSt	6470–8775	2300	122	7450
2019 Jul 7	HIRES	3130–5950	40,000	54	5100
2019 Jul 16	HIRES	4720–8995	40,000	48	7450

Note. Resolving powers are derived from FWHM measurements of arclines in comparison spectra. HIRES wavelength coverage is quoted as continuous, but there are gaps in coverage between each of the three CCDs and sometimes between red orders.

Table A2White Dwarf Kinematics

Object	π ^a (mas)	μ_{α} cos δ (mas yr ⁻¹)	μ_{δ} (mas yr ⁻¹)	RV Meas (km s ⁻¹)	Grav. Redshift (km s ⁻¹)	Syst. Vel. (km s ⁻¹)	$U = (\text{km s}^{-1})$	$V = (\text{km s}^{-1})$	$W = (\text{km s}^{-1})$
SDSS J0006+2858	6.4 ± 0.3	$+23.2 \pm 0.2$	$+13.3 \pm 0.1$	$+27 \pm 5$	30	-3 ± 5	-18	-6	+7
WD0145+234	33.9 ± 0.3	-5.2 ± 0.1	-97.6 ± 0.1	$+43 \pm 5$	35	$+9 \pm 5$	-1	-3	-16
SDSS J0347+1624	6.9 ± 0.2	$+5.7 \pm 0.2$	-62.9 ± 0.1	$+27 \pm 5$	36	-9 ± 5	+17	-36	-20
Gaia J0510+2315	15.3 ± 0.3	-44.4 ± 0.1	-38.2 ± 0.1	$+26 \pm 5$	41	-15 ± 5	+18	-2	-15
Gaia J0611-6931	6.99 ± 0.25	$+22.7 \pm 0.1$	$+100.4 \pm 0.1$	$+60 \pm 5$	41	$+19 \pm 5$	-63	-36	+5
Gaia J0644-0352	8.9 ± 0.2	$+29.9 \pm 0.1$	-24.0 ± 0.1	$+92\pm5$	41	$+51 \pm 5$	-31	-45	+5
WD0842+572	7.52 ± 0.08	-21.9 ± 0.1	-24.2 ± 0.1	$+24 \pm 5$	29	-5 ± 5	-9	-15	-12
WD1622+587	5.5 ± 0.2	$+43.2 \pm 0.1$	-128.7 ± 0.1	-17 ± 5	21	-38 ± 5	+118	-29	-27
Gaia J2100+2122	11.5 ± 0.3	$+73.7 \pm 0.1$	$+38.4 \pm 0.1$	$+3 \pm 5$	35	-32 ± 5	-42	-20	-5

Notes. "RV Meas" is the average velocity measured for individual metal and hydrogen lines in high-resolution data (see Section 3.2). "Grav. Redshift" is derived from the atmospheric parameters produced from models reported in Table 1. "Syst. Vel." is the calculated systemic velocity for each white dwarf star. We do not report nor propagate uncertainties for the gravitational redshift that could be up to 15 km s^{-1} . UVW space motions are reported relative to the Sun such that positive U is toward the Galactic center, positive V is in the direction of Galactic rotation, and positive W is toward the north Galactic pole (Johnson & Soderblom 1987).

^a For the Gaia DR2 parallax uncertainty we add in quadrature any contribution from excess astrometric noise.

Appendix B Individual Target Spectra Figures and Tables of Line Measurements

Figures B1-B33 present most of the gas disk emission features found in this work. Tables B1-B9 present gas feature measurements for each system.

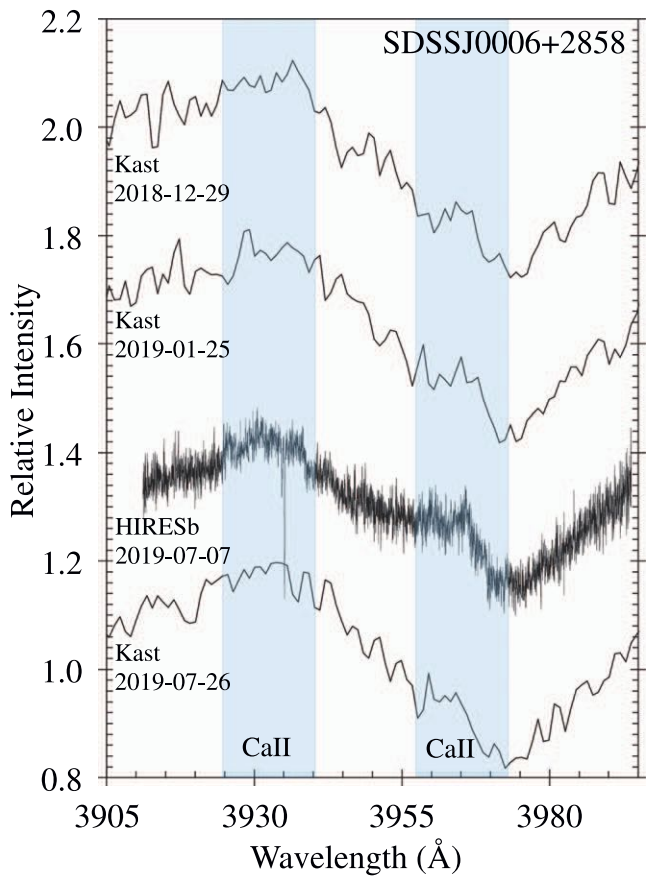


Figure B1. Ca II H+K spectra for SDSS J0006+2858. Likely emission is seen in Kast epochs, while clear emission as well as photospheric and nonphotospheric (interstellar or circumstellar) Ca II K-line absorption are seen in the HIRES data. For this and all figures shown hereafter, when there are multiple epochs present in the figure the individual epochs have been offset by an additive constant for the purposes of clarity. Wavelengths are in vacuum and shifted to the heliocentric reference frame for HIRES data, while they are in air and not shifted to the heliocentric frame for Kast data. Emission regions are marked with blue highlighted vertical bars.

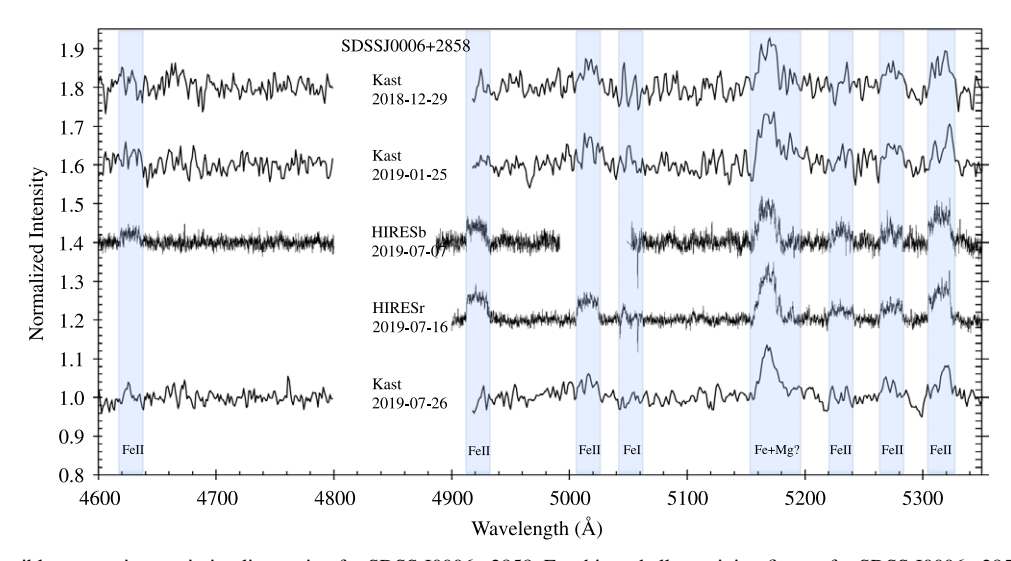


Figure B2. Iron and possibly magnesium emission line region for SDSS J0006+2858. For this and all remaining figures for SDSS J0006+2858, the continuum levels have been fit and divided into each spectrum. H β at 4863 Å is cut out of each spectrum for plotting purposes. The HIRESb spectrum contains a gap between CCDs centered around 5025 Å. HIRES data are smoothed with an 11 pixel boxcar for display purposes. Weak emission from an Fe I line near 5052 Å may be present. It is possible that there is emission from Mg I between 5150 and 5190 Å, but a clear identification is prevented due to dominating emission from Fe II in the same region.

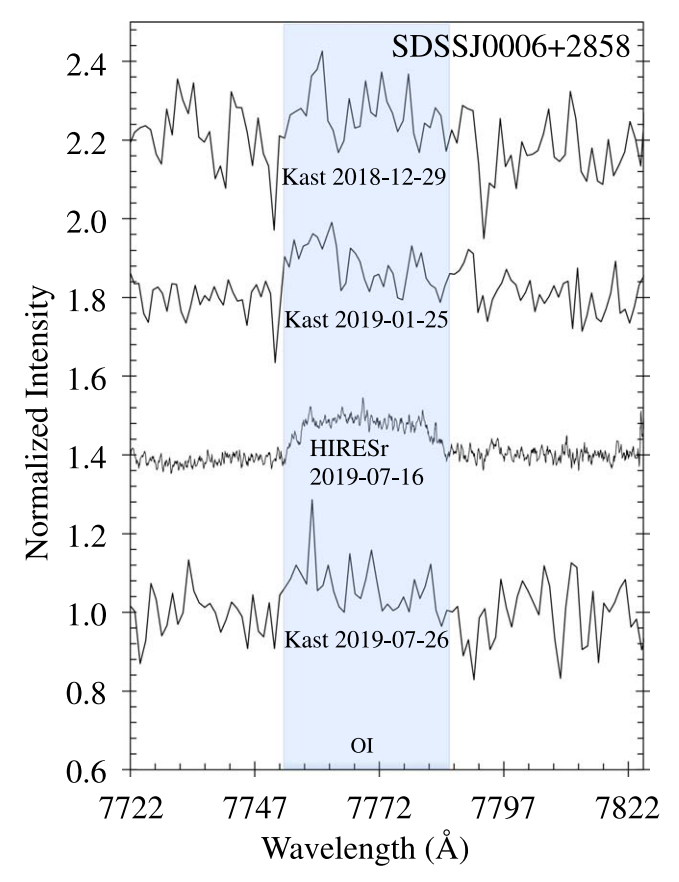


Figure B3. O I spectra for SDSS J0006+2858. HIRES spectra are smoothed with an 11 pixel boxcar. Probable emission is seen in Kast epochs, while clear emission is seen in the HIRES data.

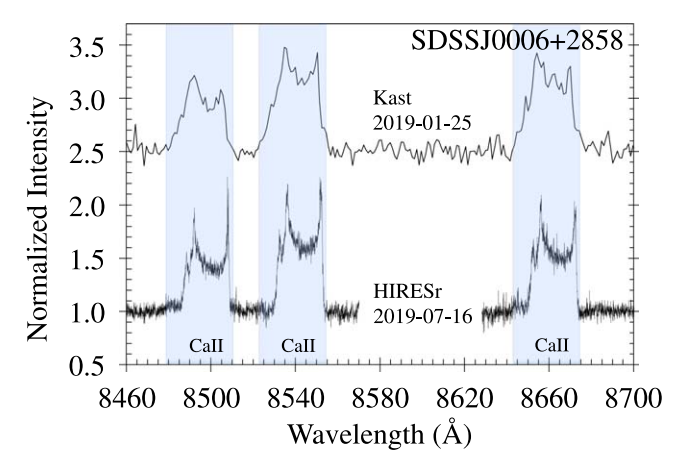


Figure B4. Ca II IRT portion of spectra for SDSS J0006+2858. Highly structured emission features are seen in the HIRES spectra, including a "third" peak on the blue shoulder of the emission feature; this "third" peak appears to also be present in the Kast epoch.

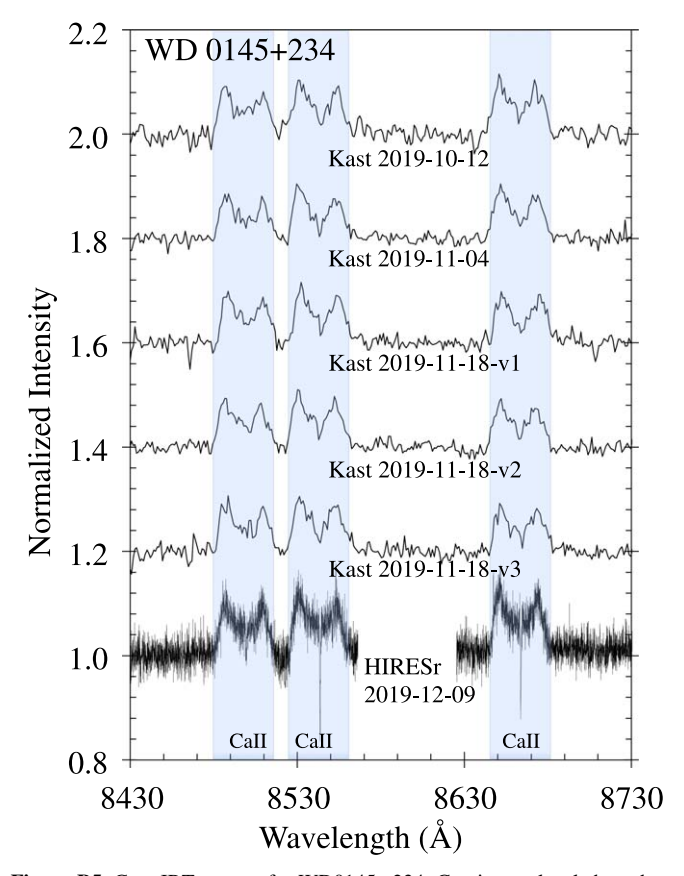


Figure B5. Ca II IRT spectra for WD0145+234. Continuum levels have been fit and divided into each spectrum for this figure. Intra-night epochs taken with the Kast are marked as "2019-11-18-v#" for three observations taken throughout the night of UT 2019 November 18; no obvious variability is seen between these or other epochs.

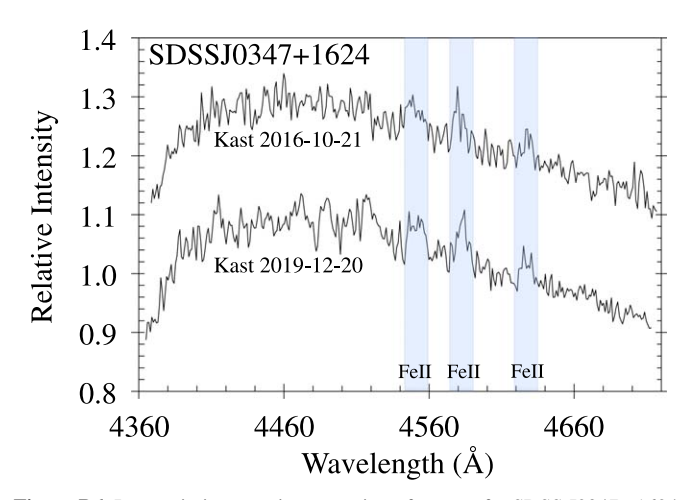


Figure B6. Iron emission seen in one region of spectra for SDSS J0347+1624. Spectra are normalized to the median flux value in this plotted range.

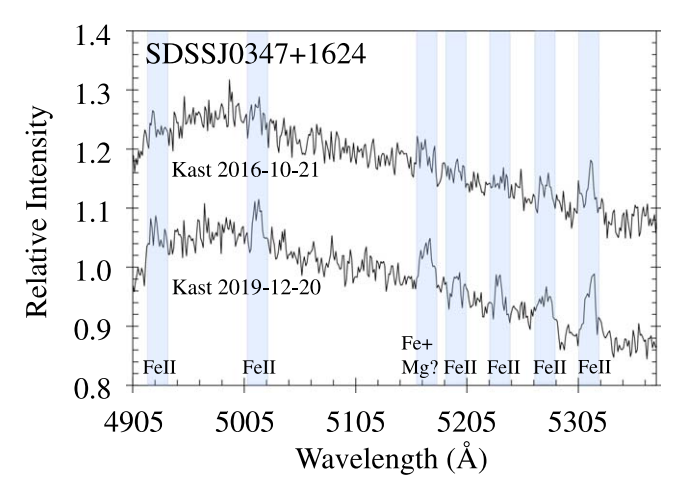


Figure B7. Iron and possibly magnesium emission seen between 4900 and 5350 Å for SDSS J0347+1624. Mg I triplet emission, if present, would be blended with the stronger Fe II λ 5169 emission. Spectra are normalized to the median flux value in this plotted range.

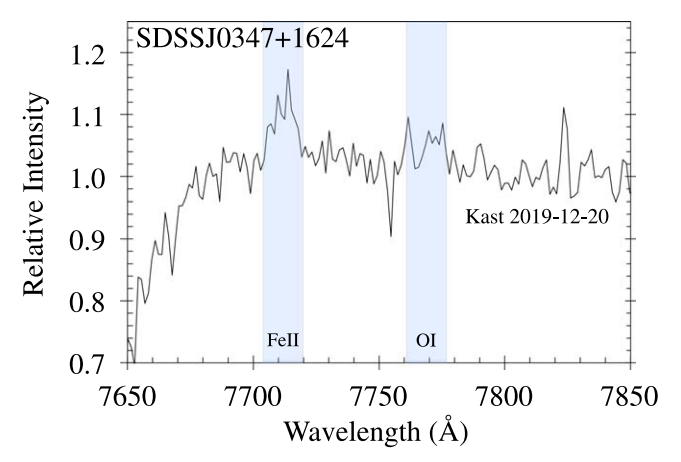


Figure B8. Oxygen and iron emission for SDSS J0347+1624. The spectrum is normalized to the median flux value in this plotted range, no continuum normalization has been done.

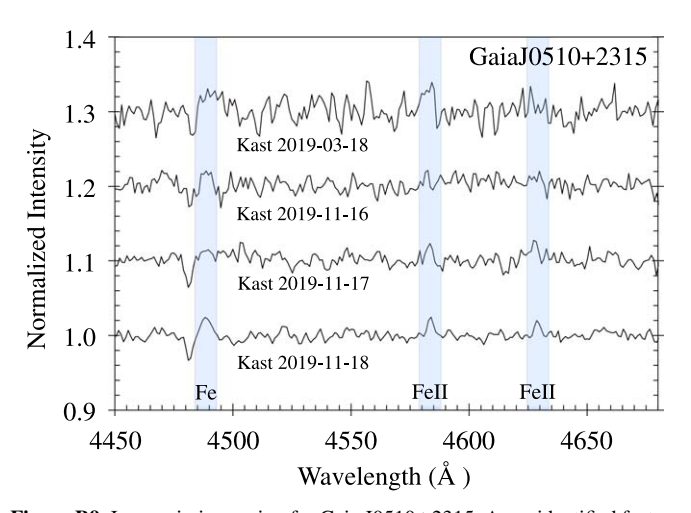


Figure B9. Iron emission region for Gaia J0510+2315. An unidentified feature (likely some combination of Fe lines) appears near 4488 Å. Spectra continuum levels have been fit and divided into each spectrum for this figure.

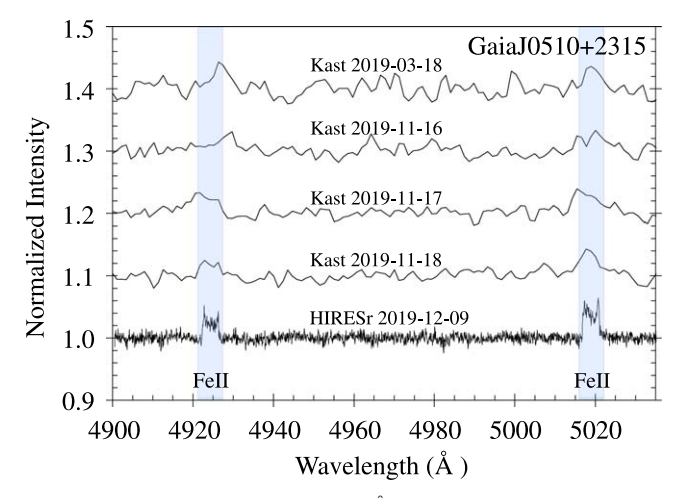


Figure B10. Iron emission near 5000 Å for Gaia J0510+2315. For all remaining plots for Gaia J0510+2315 the spectra continuum levels have been fit and divided into each spectrum and HIRES data are smoothed with a 5 pixel boxcar

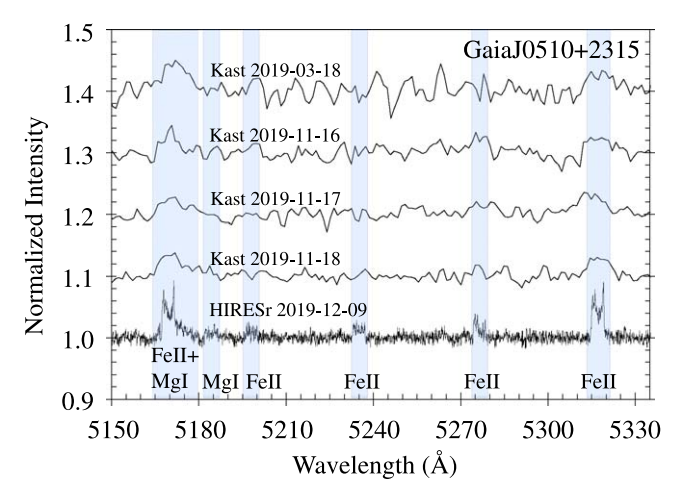


Figure B11. Iron and magnesium emission for Gaia J0510+2315.

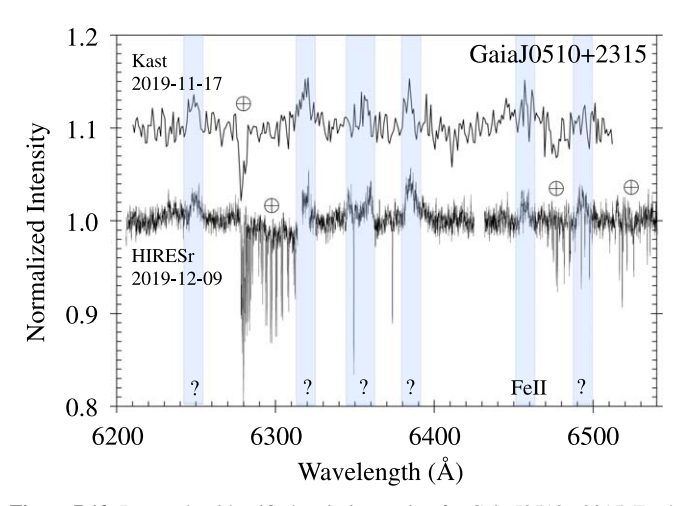


Figure B12. Iron and unidentified emission region for Gaia J0510+2315. Earth atmospheric absorption features are labeled, while strong Si II photospheric absorption lines are apparent near 6350 and 6370 Å. HIRES order gaps appear near 6315 and 6440 Å.

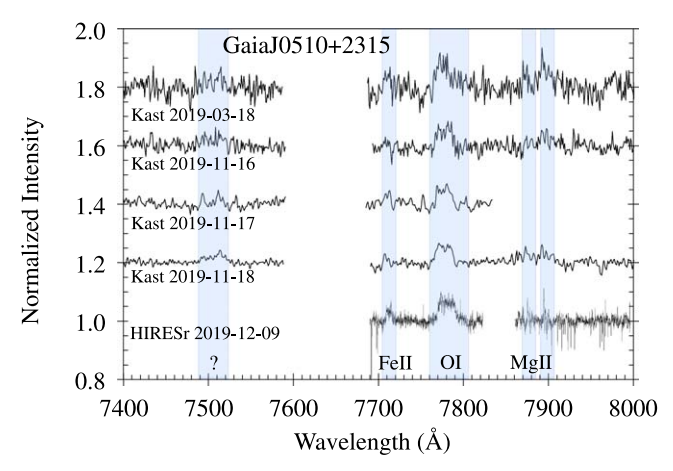


Figure B13. Iron, oxygen, and magnesium emission region for Gaia J0510 +2315. O I emission is significantly broader than that measured for all other emission lines for this star (Table B4 and Figure 2). Mg II emission is contaminated by strong telluric absorption features. An unidentified emission feature is seen near 7506 Å; this region of the spectrum is not covered by HIRES as it falls in between detectors. An inter-order gap also appears in the HIRES spectrum near 7850 Å. Strong telluric absorption near 7600 Å has been masked.

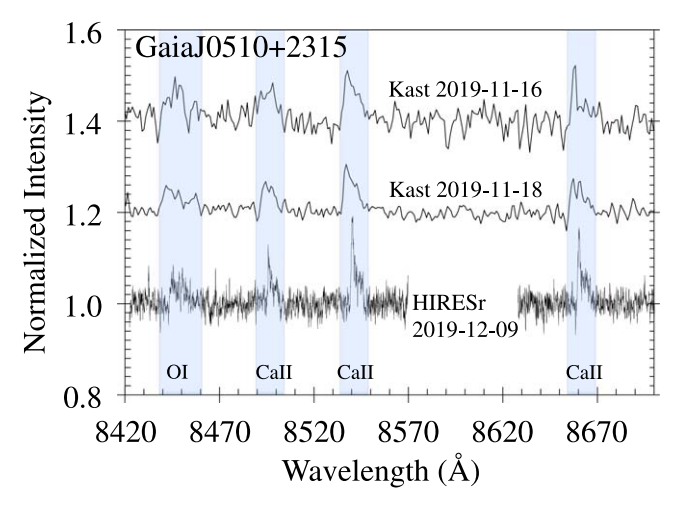


Figure B14. Oxygen and calcium emission for Gaia J0510+2315.

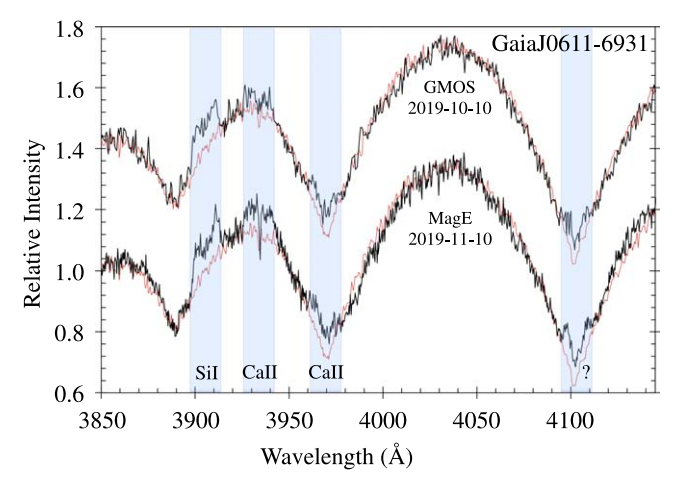


Figure B15. Blue spectral region for Gaia J0611–6931 showing several emission structures blended with strong photospheric Balmer absorption lines. Wavelengths are in air for all GMOS-S and MagE spectra shown for Gaia J0611–6931. Spectra are normalized to the median flux value in this plotted range. The red underplotted spectrum for both epochs is the DA white dwarf Gaia J0720–4250 that has atmospheric parameters similar to Gaia J0611–6931 (Table 1). Gaia J0720–4250 has $T_{\rm eff}=17,700~{\rm K}$ and $\log g=8.06~{\rm from}$ Gentile Fusillo (2019) and was observed with GMOS-S on UT 2019 November 15. Ca II H+K emission (with Ca II H emission in the Hε absorption line core) is evident as well as Ca II K absorption. Also apparent is emission from the Si I $\lambda 3905$ line. Possible unidentified emission appears to straddle the Hδ absorption line core.

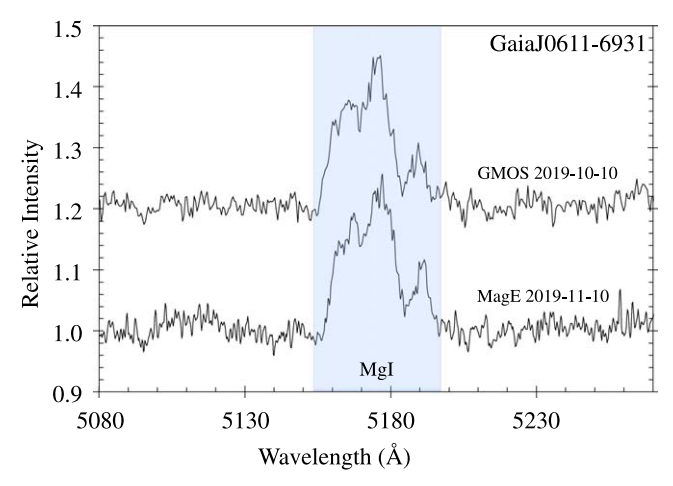


Figure B16. Magnesium spectral region for Gaia J0611-6931. Continuum levels have been fit and divided into each spectrum.

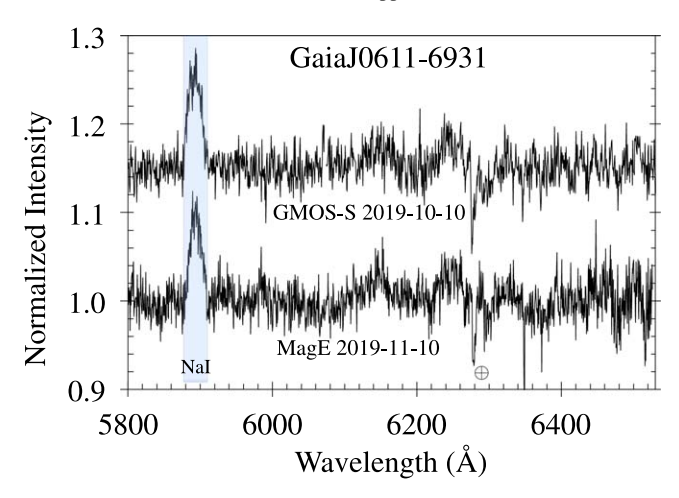


Figure B17. Sodium and possible other emission lines in Gaia J0611–6931. Continuum levels have been fit and divided into each spectrum. Emission from the Na D doublet is clearly evident. Possible emission from unidentified transitions may be present from 6100 to 6300 Å. Earth telluric absorption is marked near 6280 Å. Photospheric Si II absorption lines are detected near 6350 and 6370 Å in both spectra.

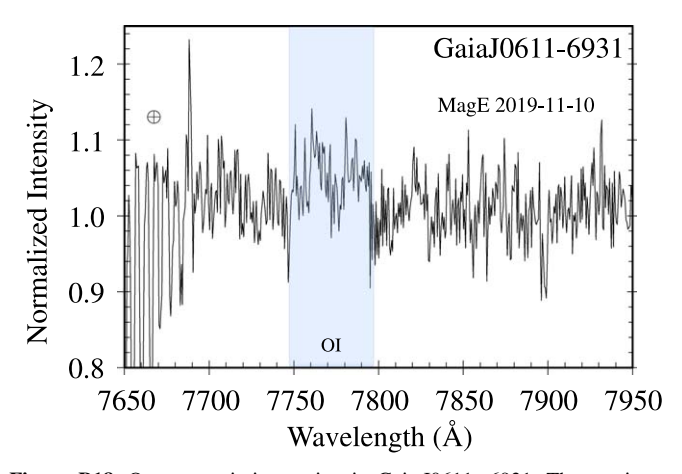


Figure B18. Oxygen emission region in Gaia J0611–6931. The continuum level has been fit and divided into the spectrum. Earth atmospheric absorption is marked.

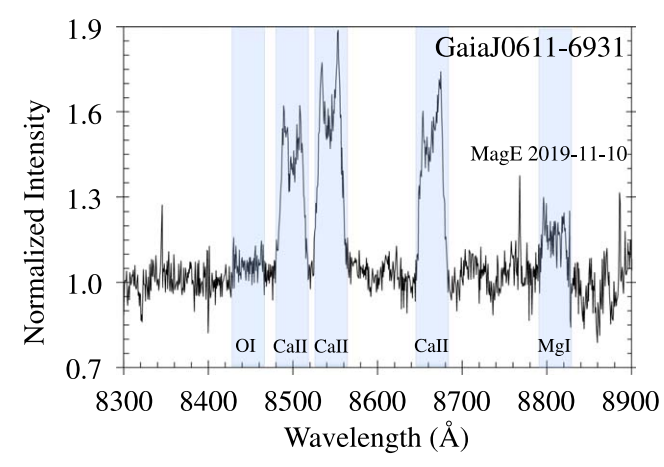


Figure B19. Calcium, oxygen, and magnesium emission lines in Gaia J0611 –6931. The continuum level has been fit and divided into the spectrum.

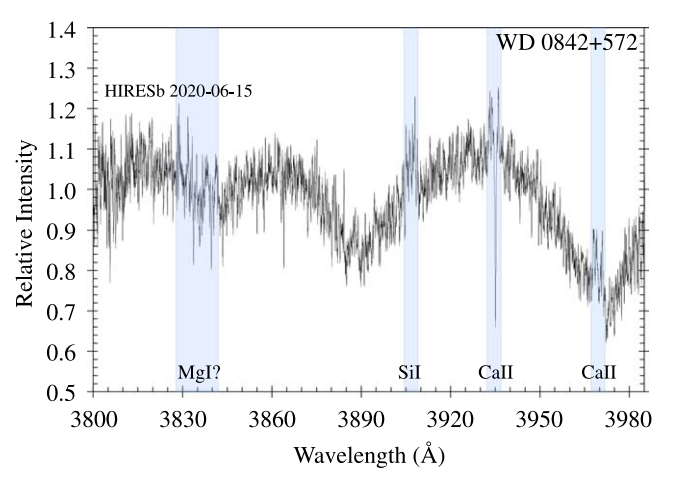


Figure B20. Blue spectral region for WD0842+572. Spectra are normalized to the median flux value in this plotted range. Ca II K emission and absorption are evident as well as Ca II H emission in the H ϵ absorption line core. Also present is Si I emission and possibly two Mg I features.

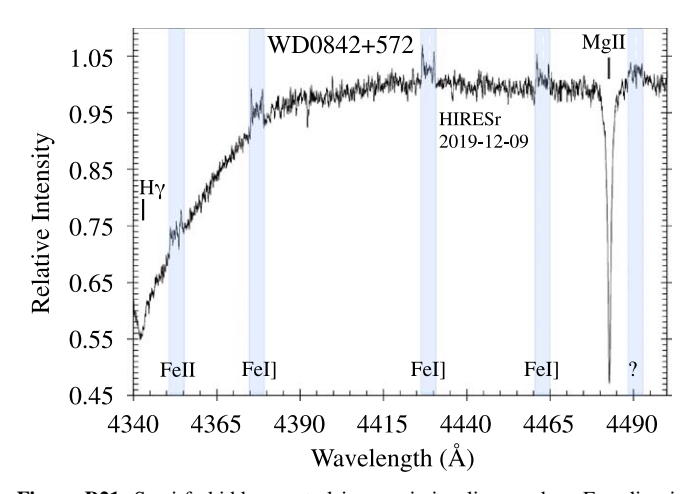


Figure B21. Semi-forbidden neutral iron emission lines and an Fe II line in WD0842+572. A weak unidentified feature appears on the red side of the strong Mg II absorption line; given the propensity for weak iron lines seen throughout the spectrum of WD0842+572, it could possibly be iron. The spectrum flux is normalized to the continuum emission level outside of the photospheric Balmer absorption.

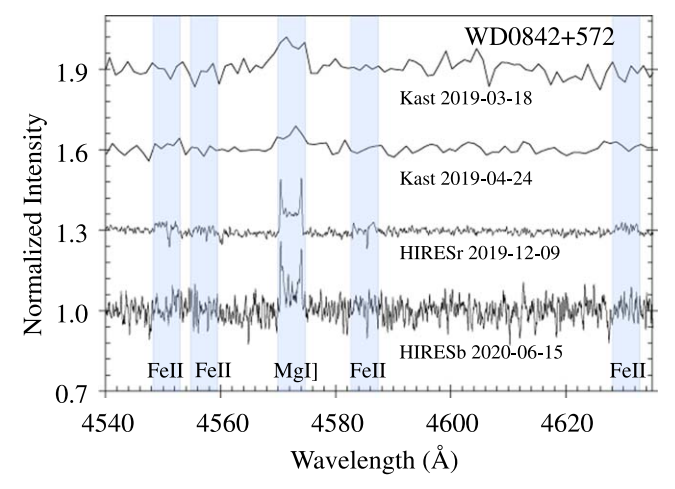


Figure B22. Iron and magnesium emission line region for WD0842+572, which features the semi-forbidden Mg I] λ 4571 line. Spectra continuum levels have been fit and divided into each spectrum. Absorption lines from Fe are present.

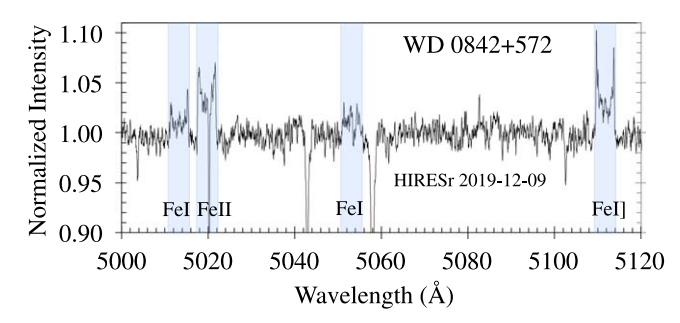


Figure B23. Another iron emission line region for WD0842+572. The spectrum continuum level has been fit and divided into the spectrum. Weak emission from an Fe I line near 5052 Å may be present. Strong photospheric absorption lines from Si (near 5040 and 5055 Å) and Fe are also seen.

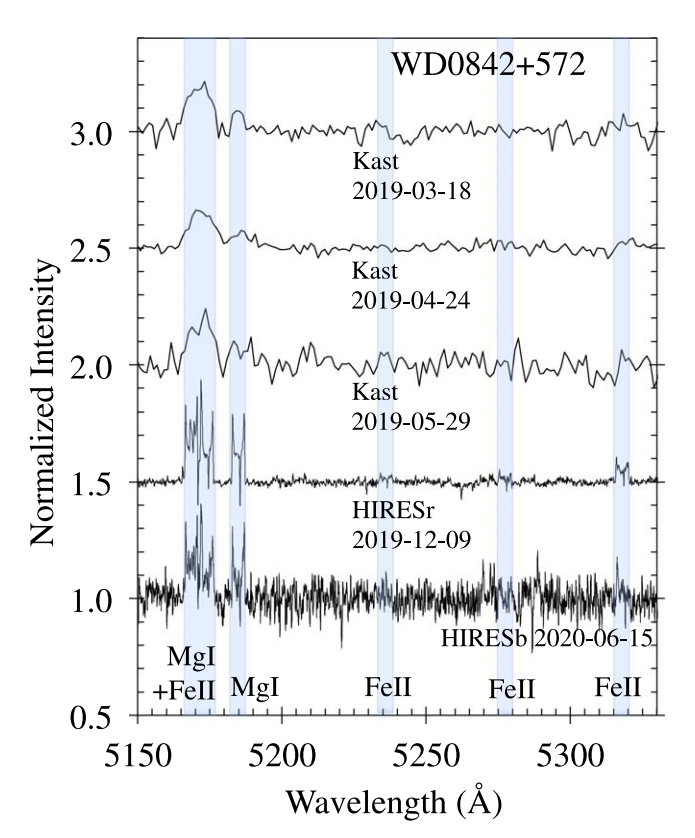


Figure B24. Iron and magnesium emission line region for WD0842+572. Based on the HIRESr spectrum, there may be numerous weak unidentified emission lines between 5200 and 5300 Å. Spectra continuum levels have been fit and divided into each spectrum. Absorption lines from Fe and the Mg I triplet are apparent.

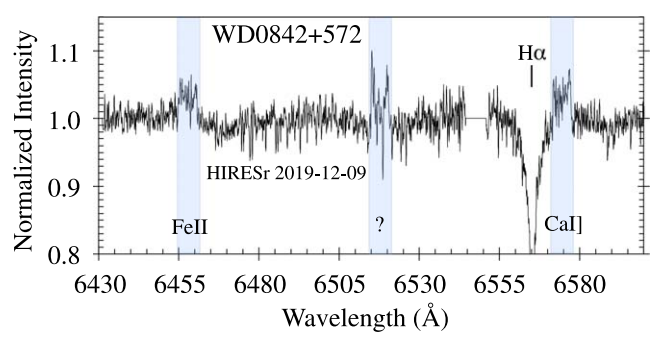


Figure B25. Iron and semi-forbidden calcium emission line region for WD0842+572. An unidentified emission line appears near 6517 Å. The spectrum continuum level and wings of the ${\rm H}\alpha$ line profile have been fit and divided into the spectrum; there is an order gap near 6550 Å.

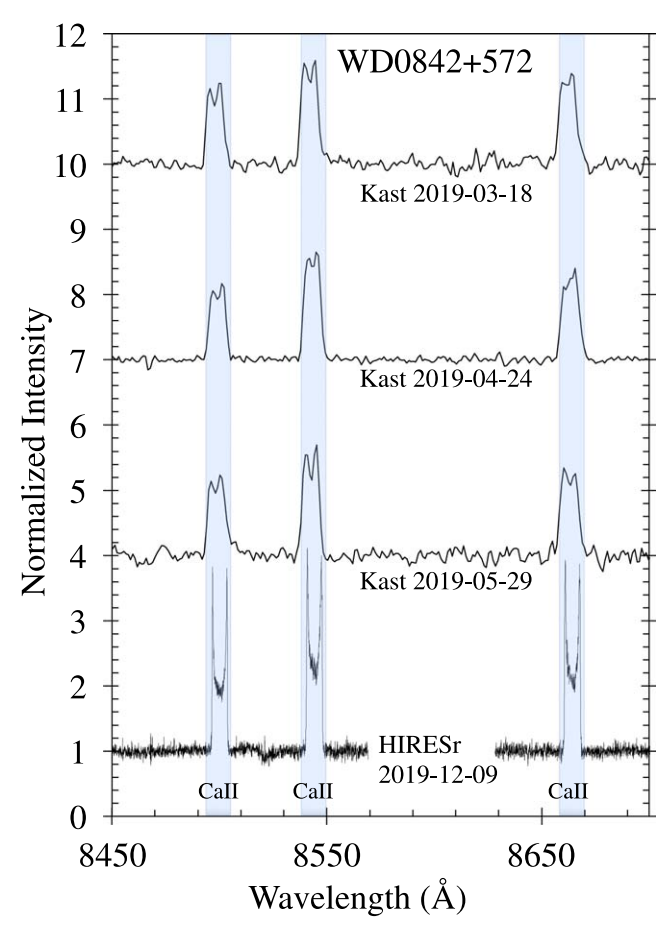


Figure B26. Ca II IRT emission line region for WD0842+572. Spectra continuum levels have been fit and divided into each spectrum.

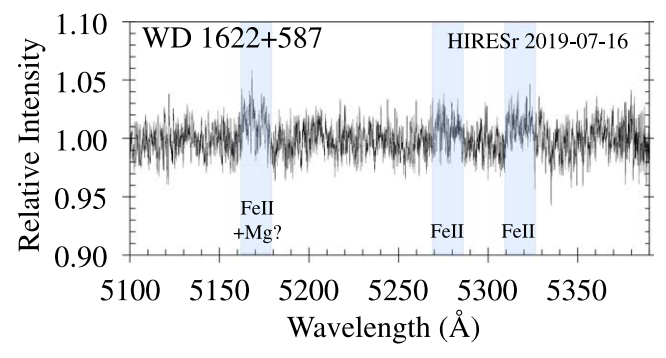


Figure B27. Iron emission region for WD1622+587. For all WD1622+587 figures the spectrum continuum levels have been fit and divided into each displayed spectrum. The spectrum shown here is smoothed with an 11 pixel boxcar for display purposes.

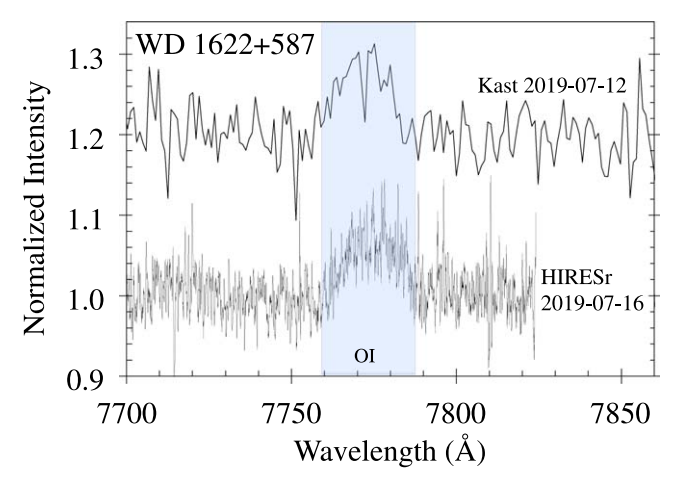


Figure B28. Oxygen emission region for WD1622+587. The HIRES spectrum has been smoothed with a 7 pixel boxcar.

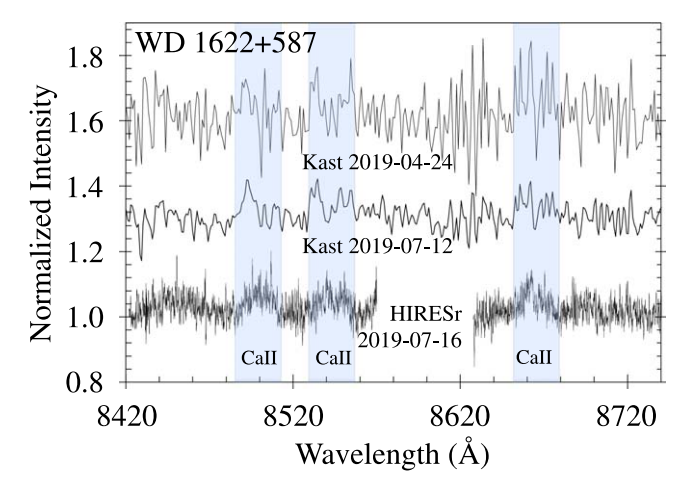


Figure B29. Calcium emission region for WD1622+587. The HIRES spectrum has been smoothed with a 7 pixel boxcar.

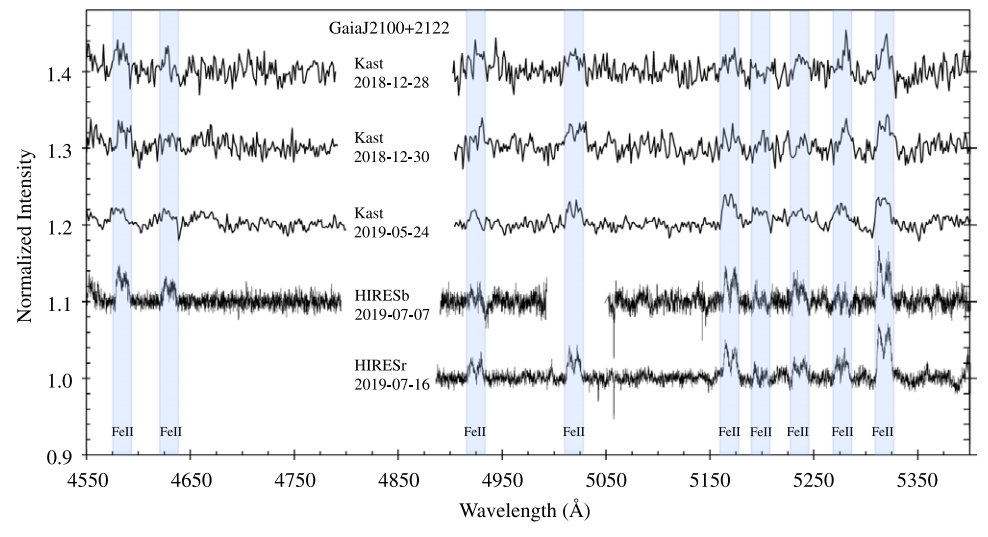


Figure B30. Iron emission region for Gaia J2100+2122. H β is cut out of each spectrum for plotting purposes, HIRESb data also feature a gap between CCDs centered around 5025 Å. For this and all figures for Gaia J2100+2122 the spectra continuum levels have been fit and divided into each spectrum displayed. The HIRES spectra in this figure are smoothed with an 11 pixel boxcar for display purposes. Si II photospheric absorption lines appear near 5040 and 5055 Å.

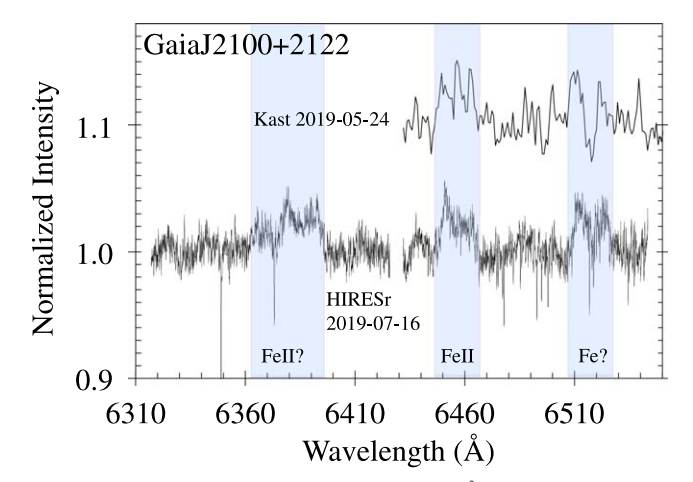


Figure B31. Another iron emission region for Gaia J2100+2122. Lines near 6382 and 6515 Å are unidentified; they may be due to Fe. The HIRES spectra are smoothed with a 7 pixel boxcar and feature an order gap near 6420 Å. Strong photospheric Si II absorption appears near 6350 and 6370 Å; other absorption lines are from Earth's atmosphere.

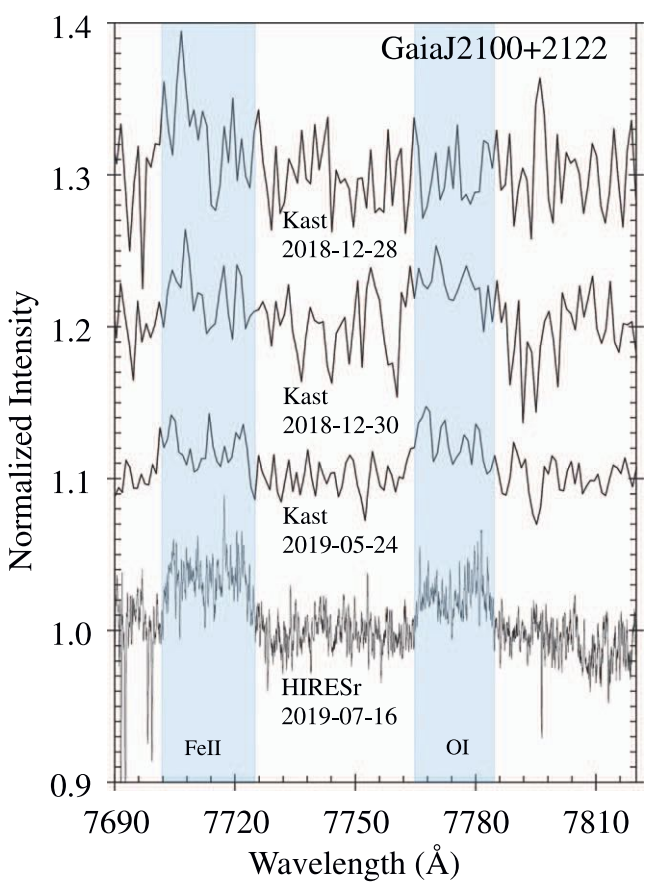


Figure B32. Oxygen and iron emission for Gaia J2100+2122.

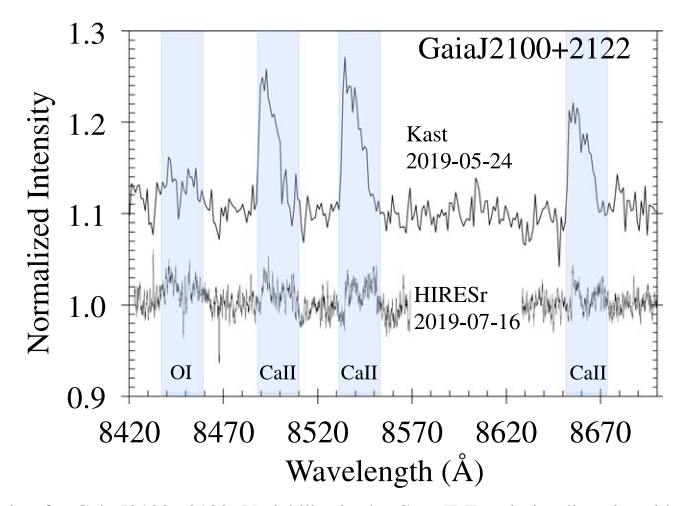


Figure B33. Calcium and oxygen emission for Gaia J2100+2122. Variability in the Ca II IRT emission lines is evident between the Kast and HIRES epochs.

Table B1SDSS J0006+2858 Emission Line Measurements

Transition	UT Date	Eq. Width (Å)	Peak Separation (km s ⁻¹)	$v_{\text{max}} \sin i $ (km s^{-1})	Full Width (km s ⁻¹)
Οι λ7772	2018 Dec 29	1.6 ± 1.2			•••
Οι λ7772	2019 Jan 25	2.4 ± 0.6	•••	•••	
Ο Ι λ7772	2019 Jul 16	2.6 ± 0.2	•••	$-825 \pm 25/300 \pm 30$	
Οι λ7772	2019 Jul 26	2.5 ± 1.1		•••	•••
Ο Ι λ8446	2019 Jul 16	0.9 ± 0.4		$-780 \pm 25/290 \pm 25$	
Ca II $\lambda 3933$	2019 Jul 7	0.5 ± 0.1		$-790 \pm 30/350 \pm 25$	1135 ± 38

Table B1 (Continued)

Transition	UT Date	Eq. Width (Å)	Peak Separation (km s ⁻¹)	$v_{\text{max}} \sin i $ (km s^{-1})	Full Width (km s ⁻¹)
Ca II λ8498	2019 Jan 25	12.0 ± 0.6	460 ± 20		1350 ± 190
Ca II $\lambda 8498$	2019 Jul 16	9.6 ± 0.3	560 ± 5	$-770 \pm 35/320 \pm 10$	1090 ± 37
Ca II λ8542	2019 Jan 25	19.2 ± 1.0	550 ± 25		1330 ± 90
Ca II $\lambda 8542$	2019 Jul 16	17.2 ± 0.2	556 ± 5	$-840 \pm 25/340 \pm 15$	1175 ± 27
Ca II $\lambda 8662$	2019 Jan 25	16.5 ± 3.1	510 ± 10		1380 ± 150
Ca II $\lambda 8662$	2019 Jul 16	13.9 ± 0.5	560 ± 5	$-780 \pm 20/330 \pm 10$	1110 ± 22
Fe II $\lambda 4629$	2019 Jul 7	0.4 ± 0.2		$-790 \pm 45/340 \pm 65$	1130 ± 80
Fe II $\lambda 4924$	2019 Jul 7	0.5 ± 0.2		$-810 \pm 45/380 \pm 90$	1190 ± 100
Fe II $\lambda 4924$	2019 Jul 16	0.9 ± 0.1		$-795 \pm 30/410 \pm 45$	1205 ± 53
Fe II $\lambda 5018$	2018 Dec 29	1.0 ± 0.5			
Fe II $\lambda 5018$	2019 Jan 25	0.7 ± 0.4			
Fe II $\lambda 5018$	2019 Jul 16	0.8 ± 0.1		$-870 \pm 30/410 \pm 50$	1280 ± 56
Fe II $\lambda 5018$	2019 Jul 26	1.2 ± 0.3			
Fe II $\lambda 5235$	2019 Jul 7	0.3 ± 0.2		•••	
Fe II $\lambda 5235$	2019 Jul 16	0.3 ± 0.1		$-860 \pm 90/365 \pm 35$	1225 ± 93
Fe II $\lambda 5276$	2018 Dec 29	0.8 ± 0.3			
Fe II $\lambda 5276$	2019 Jul 7	0.6 ± 0.2		$-790 \pm 35/325 \pm 25$	1115 ± 41
Fe II $\lambda 5276$	2019 Jul 16	0.5 ± 0.1		$-805 \pm 45/345 \pm 60$	1150 ± 73
Fe II $\lambda 5317$	2018 Dec 29	1.4 ± 0.7			
Fe II $\lambda 5317$	2019 Jan 25	1.3 ± 0.6		•••	
Fe II $\lambda 5317$	2019 Jul 7	1.2 ± 0.2		$-785 \pm 40/370 \pm 45$	1155 ± 60
Fe II $\lambda 5317$	2019 Jul 16	1.2 ± 0.1		$-790 \pm 25/335 \pm 25$	1130 ± 32
Fe II $\lambda 5317$	2019 Jul 26	1.1 ± 0.3			

Note. See Section 3.2 for descriptions of Peak Separation, $v_{\text{max}} \sin i$, and Full Width and when these measurements can be made. The two different values reported for $v_{\text{max}} \sin i$ correspond to the maximum velocity gas seen in the blue and red wings of the emission features, respectively. Full velocity width of the emission feature is the velocity extent from the blue to the red wings and is only measured when a line is not blended with another transition.

Table B2 WD0145+234 Emission Line Measurements

Transition	UT Date	Eq. Width (Å)	Peak Separation (km s ⁻¹)	$v_{\text{max}} \sin i $ (km s^{-1})	Full Width (km s ⁻¹)
Ca II λ8498	2019 Oct 12	2.1 ± 0.5	800 ± 15		1410 ± 115
Ca II $\lambda 8498$	2019 Nov 4	1.8 ± 0.2	770 ± 15	•••	1450 ± 90
Ca II $\lambda 8498$	2019 Nov 18 ^a	2.0 ± 0.2	750 ± 10	•••	1380 ± 60
Ca II $\lambda 8498$	2019 Dec 9	2.0 ± 0.2	770 ± 6	$-650 \pm 35/700 \pm 70$	1355 ± 79
Ca II $\lambda 8542$	2019 Oct 12	1.9 ± 0.5	765 ± 15	•••	1455 ± 113
Ca II $\lambda 8542$	2019 Nov 4	1.8 ± 0.2	740 ± 35		1405 ± 90
Ca II $\lambda 8542$	2019 Nov 18 ^a	2.3 ± 0.1	760 ± 10	•••	1545 ± 120
Ca II $\lambda 8542$	2019 Dec 9	1.9 ± 0.3	790 ± 6	$-655 \pm 50/650 \pm 50$	1310 ± 75
Ca II λ8662	2019 Oct 12	2.3 ± 0.3	730 ± 15		1520 ± 120
Ca II λ8662	2019 Nov 4	2.1 ± 0.3	715 ± 20		1470 ± 120
Ca II λ8662	2019 Nov 18 ^a	2.2 ± 0.2	730 ± 35		1510 ± 76
Ca II $\lambda 8662$	2019 Dec 9	1.8 ± 0.4	795 ± 10	$-630 \pm 20/650 \pm 20$	1280 ± 30

Notes. See notes to Table B1.

Table B3SDSS J0347+1624 Emission Line Measurements

Transition	UT Date	Eq. Width (Å)	Peak Separation (km s ⁻¹)	$v_{\text{max}} \sin i $ (km s^{-1})	Full Width (km s ⁻¹)
Οι λ7772	2019 Dec 20	0.4 ± 0.2			
Ca II $\lambda 8498$	2019 Dec 20	6.8 ± 0.6	300 ± 10		760 ± 75
Ca II $\lambda 8542$	2019 Dec 20	7.9 ± 0.6	280 ± 15		790 ± 80
Ca II $\lambda 8662$	2019 Dec 20	7.1 ± 0.9	280 ± 10		780 ± 75
Fe II $\lambda 4549$	2016 Oct 21	0.6 ± 0.4		•••	

^a Three exposures were taken over the course of the night. The values reported are the average of measurements made for each individual exposure with individual values for each separate exposure agreeing to within their uncertainties.

Table B3 (Continued)

Transition	UT Date	Eq. Width (Å)	Peak Separation (km s ⁻¹)	$v_{\text{max}} \sin i $ (km s^{-1})	Full Width (km s ⁻¹)
Fe II λ4549	2019 Dec 20	0.5 ± 0.3			
Fe II $\lambda 4584$	2016 Oct 21	0.5 ± 0.2			
Fe II $\lambda 4584$	2019 Dec 20	0.5 ± 0.2		•••	
Fe II $\lambda 4629$	2016 Oct 21	0.3 ± 0.2			
Fe II $\lambda 4629$	2019 Dec 20	0.3 ± 0.1			
Fe II $\lambda 4924$	2016 Oct 21	0.2 ± 0.1			
Fe II $\lambda 4924$	2019 Dec 20	0.4 ± 0.2			
Fe II $\lambda 5018$	2016 Oct 21	0.2 ± 0.1			
Fe II $\lambda 5018$	2019 Dec 20	0.4 ± 0.1			
Fe II $\lambda 5235$	2019 Dec 20	0.4 ± 0.2			
Fe II $\lambda 5276$	2016 Oct 21	0.3 ± 0.1			
Fe II $\lambda 5276$	2019 Dec 20	0.7 ± 0.2			
Fe II $\lambda 5317$	2019 Oct 21	0.7 ± 0.4			
Fe II $\lambda 5317$	2019 Dec 20	1.3 ± 0.3			_

Note. See notes to Table B1.

Table B4Gaia J0510+2315 Emission Line Measurements

Transition	UT Date	Eq. Width (Å)	Peak Separation (km s ⁻¹)	$v_{\text{max}} \sin i $ (km s^{-1})	Full Width (km s ⁻¹)
Οι λ7772	2019 Mar 18	2.2 ± 1.1	•••		
Ο Ι λ7772	2019 Nov 16	1.3 ± 0.4		•••	
Ο Ι λ7772	2019 Nov 17	1.4 ± 0.4	•••	•••	
Ο Ι λ7772	2019 Nov 18 ^a	1.3 ± 0.3	•••	•••	
Ο Ι λ7772	2019 Dec 9	1.0 ± 0.2	•••	$-185 \pm 25/650 \pm 60$	•••
Ο Ι λ8446	2019 Nov 16	0.6 ± 0.4	•••	•••	
Ο Ι λ8446	2019 Nov 18 ^a	0.6 ± 0.2	•••	•••	
Ο Ι λ8446	2019 Dec 9	0.4 ± 0.1	•••	$-185 \pm 20/500 \pm 200$	•••
Mg I λ5184	2019 Dec 9	0.06 ± 0.03	•••	$-195 \pm 60/115 \pm 60$	310 ± 82
Mg II λ 7896	2019 Dec 9	0.2 ± 0.1		$-175 \pm 25/100 \pm 75$	285 ± 80
Ca II λ8498	2019 Nov 16	0.6 ± 0.4			
Ca II λ8498	2019 Nov 18 ^a	0.4 ± 0.1			
Ca II λ8498	2019 Dec 9	0.3 ± 0.1		$-190 \pm 30/115 \pm 45$	305 ± 54
Ca II $\lambda 8542$	2019 Nov 16	0.9 ± 0.3		•••	
Ca II $\lambda 8542$	2019 Nov 18 ^a	0.7 ± 0.2		•••	
Ca II $\lambda 8542$	2019 Dec 9	0.6 ± 0.1	•••	$-180 \pm 15/100 \pm 20$	280 ± 23
Ca II λ8662	2019 Nov 16	0.7 ± 0.4		•••	
Ca II $\lambda 8662$	2019 Nov 18 ^a	0.4 ± 0.2	•••	•••	
Ca II λ8662	2019 Dec 9	0.5 ± 0.1	•••	$-175 \pm 12/90 \pm 15$	265 ± 18
Fe II $\lambda 4924$	2019 Nov 17	0.2 ± 0.1	•••	•••	
Fe II $\lambda 4924$	2019 Nov 18 ^a	0.3 ± 0.2	•••	•••	
Fe II $\lambda 4924$	2019 Dec 9	0.15 ± 0.03	•••	$-185 \pm 16/110 \pm 20$	295 ± 24
Fe II $\lambda 5018$	2019 Mar 18	0.2 ± 0.1	•••	•••	
Fe II $\lambda 5018$	2019 Nov 16	0.3 ± 0.2	•••	•••	
Fe II $\lambda 5018$	2019 Nov 17	0.3 ± 0.2	•••	•••	•••
Fe II $\lambda 5018$	2019 Nov 18 ^a	0.3 ± 0.1	•••	•••	•••
Fe II $\lambda 5018$	2019 Dec 9	0.20 ± 0.03	•••	$-180 \pm 13/115 \pm 30$	295 ± 33
Fe II $\lambda 5235$	2019 Dec 9	0.10 ± 0.03	•••	$-190 \pm 35/115 \pm 60$	305 ± 67
Fe II $\lambda 5276$	2019 Dec 9	0.10 ± 0.05	•••	$-200 \pm 40/105 \pm 60$	305 ± 70
Fe II $\lambda 5317$	2019 Mar 18	0.3 ± 0.2		•••	
Fe II $\lambda 5317$	2019 Nov 17	0.3 ± 0.2	•••	•••	
Fe II $\lambda 5317$	2019 Nov 18 ^a	0.25 ± 0.05	•••	•••	•••
Fe II $\lambda 5317$	2019 Dec 9	0.25 ± 0.05	•••	$-215\pm40/140\pm45$	355 ± 60

Notes. See notes to Table B1.

^a Two exposures were taken over the course of the night. The values reported are the average of measurements made for each individual exposure with individual values for each separate exposure agreeing to within their uncertainties.

Table B5Gaia J0611-6931 Emission Line Measurements

Transition	UT Date	Eq. Width (Å)	Peak Separation (km s ⁻¹)	$v_{\rm max} \sin i \ ({ m km s}^{-1})$	Full Width (km s ⁻¹)
Οι λ7772	2019 Nov 10	2.7 ± 1.1	•••	$-790 \pm 250/775 \pm 60$	•••
Οι λ8446	2019 Nov 10	1.7 ± 0.8		$-615 \pm 70/700 \pm 70$	
Na I λ5890	2019 Oct 10	2.3 ± 0.3		•••	
Na I $\lambda 5890$	2019 Nov 10	1.8 ± 0.3		$-680 \pm 100/800 \pm 180$	
Mg I λ5167	2019 Oct 10	4.5 ± 0.6		•••	
Mg I λ5167	2019 Nov 10	5.6 ± 0.8		$-735 \pm 75/755 \pm 115$	
Mg I λ8806	2019 Nov 10	4.8 ± 1.4		$-630 \pm 60/670 \pm 50$	1300 ± 78
Si I λ3905	2019 Oct 10	1.5 ± 0.3		•	•••
Si I λ3905	2019 Nov 10	1.5 ± 0.5		$-675 \pm 115/670 \pm 75$	1345 ± 139
Ca II $\lambda 3933$	2019 Oct 10	0.8 ± 0.4			•••
Ca II $\lambda 3933$	2019 Nov 10	1.5 ± 0.5		$-790 \pm 115/845 \pm 75$	1635 ± 138
Ca II λ8498	2019 Nov 10	12.9 ± 1.2	625 ± 20	$-680 \pm 25/690 \pm 35$	1370 ± 43
Ca II λ8542	2019 Nov 10	17.3 ± 1.7	670 ± 10	$-670 \pm 25/730 \pm 50$	1400 ± 56
Ca II $\lambda 8662$	2019 Nov 10	16.9 ± 1.5	680 ± 10	$-715 \pm 85/735 \pm 50$	1450 ± 100

Note. See notes to Table B1.

Table B6Gaia J0644-0352 Emission Line Measurements

Transition	UT Date	Eq. Width (Å)	Peak Separation (km s ⁻¹)	$v_{\text{max}} \sin i $ (km s^{-1})	Full Width (km s ⁻¹)
Ca II λ8498	2019 Dec 9	1.5 ± 0.4		$-370 \pm 45/530 \pm 105$	900 ± 115
Ca II $\lambda 8542$	2019 Dec 9	1.0 ± 0.4		$-370 \pm 60/460 \pm 40$	835 ± 72
Ca II $\lambda 8662$	2019 Dec 9	1.1 ± 0.5	•••	$-330 \pm 25/475 \pm 30$	805 ± 39

Note. See notes to Table B1.

Table B7 WD0842+572 Emission Line Measurements

Mg I] $\lambda 4571$ 2019	9 Mar 18 9 Apr 24 9 Dec 9	0.6 ± 0.2 0.4 ± 0.1	•••	•••	
C ,	•				•••
Ma II \4571 201	9 Dec 9		•••	•••	
Mg IJ 743/1 201		0.4 ± 0.1	240 ± 5	$-150 \pm 20/140 \pm 14$	290 ± 24
Mg I $\lambda 5184$ 201	9 Dec 9	0.6 ± 0.1	230 ± 5	$-135 \pm 11/135 \pm 10$	270 ± 14
Si I λ3905 202	0 Jun 15	0.5 ± 0.3	•••	$-180 \pm 45/150 \pm 20$	330 ± 50
Ca I] $\lambda 6573$ 201	9 Dec 9	0.2 ± 0.1	230 ± 5	$-140 \pm 12/135 \pm 10$	275 ± 15
Ca II λ3933 202	0 Jun 15	0.1 ± 0.1		$-170 \pm 40/120 \pm 25$	290 ± 47
Ca II λ8498 2019	9 Mar 18	10.1 ± 1.1	170 ± 15		515 ± 70
Ca II λ8498 2019	9 Apr 24	9.0 ± 0.8	155 ± 15		500 ± 60
Ca II λ8498 2019	May 29	10.7 ± 1.7	165 ± 15		630 ± 140
Ca II λ8498 201	9 Dec 9	9.3 ± 0.8	230 ± 5	$-140 \pm 10/140 \pm 10$	280 ± 12
Ca II λ8542 2019	9 Mar 18	13.0 ± 1.8	165 ± 15		675 ± 150
Ca II λ8542 2019	9 Apr 24	13.1 ± 1.0	140 ± 15	•••	545 ± 90
Ca II λ8542 2019	9 May 29	13.1 ± 1.7	155 ± 15	•••	545 ± 80
Ca II λ8542 201	9 Dec 9	12.5 ± 1.0	225 ± 5	$-160 \pm 18/160 \pm 20$	320 ± 26
Ca II λ8662 2019	9 Mar 18	12.5 ± 2.6	•••		690 ± 115
Ca II λ8662 2019	9 Apr 24	12.0 ± 1.0	•••	•••	630 ± 95
Ca II λ8662 2019	9 May 29	12.8 ± 5.0	160 ± 15	•••	710 ± 200
Ca II λ8662 201	9 Dec 9	11.8 ± 0.8	230 ± 5	$-155 \pm 15/150 \pm 10$	305 ± 17
Fe I] $\lambda 4376$ 201	9 Dec 9	0.2 ± 0.1	•••	$-135 \pm 11/140 \pm 11$	275 ± 15
Fe I] $\lambda 4427$ 201	9 Dec 9	0.13 ± 0.06		$-150 \pm 20/140 \pm 14$	290 ± 25
Fe I] $\lambda 4462$ 201	9 Dec 9	0.10 ± 0.08		$-155 \pm 20/145 \pm 14$	300 ± 22
Fe I $\lambda 5012$ 201	9 Dec 9	0.13 ± 0.05		$-160 \pm 20/135 \pm 13$	295 ± 22
Fe I] $\lambda 5110$ 201	9 Dec 9	0.2 ± 0.1	235 ± 10	$-145 \pm 13/135 \pm 15$	280 ± 19
Fe II λ4629 201	9 Dec 9	0.10 ± 0.05		$-200 \pm 70/160 \pm 35$	360 ± 78

Table B7 (Continued)

Transition	UT Date	Eq. Width (Å)	Peak Separation (km s ⁻¹)	$v_{\text{max}} \sin i $ (km s^{-1})	Full Width (km s ⁻¹)
Fe II λ4924	2019 Dec 9	0.2 ± 0.1		$-140 \pm 16/130 \pm 13$	270 ± 20
Fe II $\lambda 5018$	2019 Dec 9	0.14 ± 0.07	230 ± 10	$-150 \pm 15/130 \pm 10$	280 ± 18
Fe II $\lambda 5317$	2019 Dec 9	0.3 ± 0.1		$-135 \pm 12/145 \pm 18$	280 ± 20

Note. See notes to Table B1.

Table B8WD1622+587 Emission Line Measurements

Transition	UT Date	Eq. Width (Å)	Peak Separation (km s ⁻¹)	$v_{\text{max}} \sin i $ (km s^{-1})	Full Width (km s ⁻¹)
Οι λ7772	2019 Jul 12	1.3 ± 0.1		•••	•••
Οι λ7772	2019 Jul 16	1.9 ± 0.7		$-460 \pm 95/445 \pm 95$	
Ca II λ8498	2019 Jul 16	2.4 ± 0.6		$-420 \pm 105/430 \pm 70$	850 ± 127
Ca II λ8542	2019 Jul 16	2.7 ± 1.3		$-550 \pm 140/480 \pm 105$	1030 ± 175
Ca II λ8662	2019 Jul 16	1.1 ± 0.9		$-300 \pm 120/470 \pm 70$	770 ± 139
Fe II $\lambda 5276$	2019 Jul 16	0.3 ± 0.2		$-400 \pm 115/570 \pm 115$	970 ± 161
Fe II $\lambda 5317$	2019 Jul 16	0.4 ± 0.2		$-445 \pm 115/540 \pm 140$	985 ± 181

Note. See notes to Table B1.

Table B9Gaia J2100+2122 Emission Line Measurements

Transition	UT Date	Eq. Width (Å)	Peak Separation (km s ⁻¹)	$v_{ m max} \sin i \ ({ m km \ s}^{-1})$	Full Width (km s ⁻¹)
Οι λ7772	2019 May 24	0.4 ± 0.2			
Οι λ7772	2019 Jul 16	0.6 ± 0.2	•••	$-390 \pm 60/350 \pm 80$	•••
Ca II $\lambda 8498$	2019 May 24	1.6 ± 0.2	•••	•••	740 ± 190
Ca II $\lambda 8498$	2019 Jul 16	0.8 ± 0.2	•••	$-385 \pm 80/460 \pm 70$	845 ± 105
Ca II $\lambda 8542$	2019 May 24	1.7 ± 0.3	•••	•••	795 ± 115
Ca II $\lambda 8542$	2019 Jul 16	0.5 ± 0.1	•••	$-455 \pm 140/480 \pm 140$	935 ± 199
Ca II $\lambda 8662$	2019 May 24	1.3 ± 0.1		***	780 ± 145
Ca II $\lambda 8662$	2019 Jul 16	0.3 ± 0.2	•••	$-405 \pm 105/465 \pm 70$	870 ± 125
Fe II $\lambda 4584$	2019 Jul 7	0.3 ± 0.1		$-450 \pm 45/520 \pm 45$	970 ± 65
Fe II $\lambda 4629$	2019 Jul 7	0.2 ± 0.1		$-470 \pm 90/430 \pm 100$	900 ± 133
Fe II $\lambda 4924$	2019 Jul 7	0.2 ± 0.1	•••	$-400 \pm 90/470 \pm 120$	870 ± 152
Fe II $\lambda 4924$	2019 Jul 16	0.2 ± 0.1		$-530 \pm 90/450 \pm 70$	980 ± 117
Fe II $\lambda 5018$	2018 Dec 28	0.3 ± 0.2			
Fe II $\lambda 5018$	2018 Dec 30	0.6 ± 0.2		***	
Fe II $\lambda 5018$	2019 May 24	0.25 ± 0.15	•••	•••	•••
Fe II $\lambda 5018$	2019 Jul 16	0.3 ± 0.1	•••	$-480 \pm 50/415 \pm 45$	895 ± 66
Fe II $\lambda 5169$	2018 Dec 28	0.3 ± 0.2	•••	•••	
Fe II $\lambda 5169$	2018 Dec 30	0.3 ± 0.2	•••	•••	
Fe II $\lambda 5169$	2019 May 24	0.5 ± 0.1	•••	•••	•••
Fe II $\lambda 5169$	2019 Jul 7	0.3 ± 0.2	•••	$-430 \pm 60/470 \pm 60$	900 ± 82
Fe II $\lambda 5169$	2019 Jul 16	0.4 ± 0.1	475 ± 12	$-460 \pm 60/425 \pm 35$	885 ± 68
Fe II $\lambda 5235$	2019 Jul 7	0.3 ± 0.1	•••	$-510 \pm 160/520 \pm 115$	1030 ± 197
Fe II $\lambda 5235$	2019 Jul 16	0.3 ± 0.1	•••	$-465 \pm 105/530 \pm 100$	995 ± 144
Fe II $\lambda 5276$	2018 Dec 28	0.4 ± 0.2	•••	•••	
Fe II $\lambda 5276$	2018 Dec 30	0.4 ± 0.1	•••	•••	
Fe II $\lambda 5276$	2019 May 24	0.3 ± 0.2	•••	•••	•••
Fe II $\lambda 5276$	2019 Jul 7	0.2 ± 0.1	•••	$-445\pm115/430\pm115$	875 ± 161
Fe II $\lambda 5276$	2019 Jul 16	0.4 ± 0.1	460 ± 10	$-470 \pm 80/490 \pm 85$	960 ± 116
Fe II $\lambda 5317$	2018 Dec 28	0.6 ± 0.1	•••	•••	
Fe II $\lambda 5317$	2018 Dec 30	0.6 ± 0.2			•••

Table B9 (Continued)

Transition	UT Date	Eq. Width (Å)	Peak Separation (km s ⁻¹)	$v_{\text{max}} \sin i $ (km s^{-1})	Full Width (km s ⁻¹)
Fe II λ5317	2019 May 24	0.6 ± 0.1			
Fe II $\lambda 5317$	2019 Jul 7	0.6 ± 0.2	475 ± 15	$-495 \pm 85/470 \pm 60$	965 ± 105
Fe II $\lambda 5317$	2019 Jul 16	0.7 ± 0.1	475 ± 15	$-510 \pm 85/475 \pm 30$	985 ± 90

Note. See notes to Table B1.

ORCID iDs

Carl Melis https://orcid.org/0000-0001-9834-7579
Beth Klein https://orcid.org/0000-0001-5854-675X
Alexandra E. Doyle https://orcid.org/0000-0003-0053-3854
Alycia Weinberger https://orcid.org/0000-0001-6654-7859
B. Zuckerman https://orcid.org/0000-0001-6809-3045

References

```
Balayan, S. K. 1997a, Ap, 40, 101
Balayan, S. K. 1997b, Ap, 40, 211
Bear, E., & Soker, N. 2013, NewA, 19, 56
Bédard, A., Bergeron, P., Brassard, P., & Fontaine, G. 2020, ApJ, 901, 93
Bergeron, P., Dufour, P., Fontaine, G., et al. 2019, ApJ, 876, 67
Bergeron, P., Saffer, R. A., & Liebert, J. 1992, ApJ, 394, 228
Bochkarev, K. V., & Rafikov, R. R. 2011, ApJ, 741, 36
Bognár, Z., Kalup, C., Sódor, Á., Charpinet, S., & Hermes, J. J. 2018,
         AS, 478, 2676
Brinkworth, C., Gaensicke, B., Girven, J., et al. 2012, ApJ, 750, 86
Cauley, P. W., Farihi, J., Redfield, S., et al. 2018, ApJL, 852, L22
Debes, J. H., & Sigurdsson, S. 2002, ApJ, 572, 556
Dennihy, E., Clemens, J. C., Dunlap, B. H., et al. 2018, ApJ, 854, 40
Dennihy, E., Xu, S., Lai, S., et al. 2020, ApJ, in press (arXiv:2010.03693)
Dufour, P., Bergeron, P., & Fontaine, G. 2005, ApJ, 627, 404
Dufour, P., Bergeron, P., Liebert, J., et al. 2007, ApJ, 663, 1291
Dufour, P., Kilic, M., Fontaine, G., et al. 2010, ApJ, 719, 803
Dufour, P., Kilic, M., Fontaine, G., et al. 2012, ApJ, 749, 6
Farihi, J. 2016, NewAR, 71, 9
Farihi, J., Gänsicke, B. T., & Koester, D. 2013, Sci, 342, 218
Farihi, J., Gänsicke, B. T., Steele, P. R., et al. 2012, MNRAS, 421, 1635
Farihi, J., Jura, M., & Zuckerman, B. 2009, ApJ, 694, 805
Farihi, J., van Lieshout, R., Cauley, P. W., et al. 2018, MNRAS, 481, 2601
Florez, L., & Wilson, D. 2020, BAAS, 52, 1
Fortin-Archambault, M., Dufour, P., & Xu, S. 2020, ApJ, 888, 47
Frewen, S. F. N., & Hansen, B. M. S. 2014, MNRAS, 439, 2442
Gänsicke, B. T., Koester, D., Farihi, J., et al. 2012, MNRAS, 424, 333
Gänsicke, B. T., Koester, D., Marsh, T. R., Rebassa-Mansergas, A., &
   Southworth, J. 2008, MNRAS, 391, L103
Gänsicke, B. T., Marsh, T. R., & Southworth, J. 2007, MNRAS, 380, L35
Gänsicke, B. T., Marsh, T. R., Southworth, J., & Rebassa-Mansergas, A. 2006,
Gänsicke, B. T., Schreiber, M. R., Toloza, O., et al. 2019, Natur, 576, 61
Genest-Beaulieu, C., & Bergeron, P. 2019a, ApJ, 871, 169
Genest-Beaulieu, C., & Bergeron, P. 2019b, ApJ, 882, 106
Gentile Fusillo, N. P., Gänsicke, B. T., Farihi, J., et al. 2017, MNRAS,
   468, 971
Gentile Fusillo, N. P., Tremblay, P.-E., Gänsicke, B. T., et al. 2019, MNRAS,
   482, 4570
Gianninas, A., Bergeron, P., & Fontaine, G. 2006, AJ, 132, 831
Gianninas, A., Bergeron, P., & Ruiz, M. T. 2011, ApJ, 743, 138
Grishin, E., & Veras, D. 2019, MNRAS, 489, 168
Guo, J., Tziamtzis, A., Wang, Z., et al. 2015, ApJL, 810, L17
Hartmann, S., Nagel, T., Rauch, T., & Werner, K. 2011, A&A, 530, A7
Hartmann, S., Nagel, T., Rauch, T., & Werner, K. 2016, A&A, 593, A67
Hook, I. M., Jørgensen, I., Allington-Smith, J. R., et al. 2004, PASP, 116, 425
Horne, K., & Marsh, T. R. 1986, MNRAS, 218, 761
Johnson, D. R. H., & Soderblom, D. R. 1987, AJ, 93, 864
Jura, M. 2003, ApJL, 584, L91
Jura, M. 2008, AJ, 135, 1785
```

```
Kelson, D. D. 2003, PASP, 115, 688
Kelson, D. D., Illingworth, G. D., van Dokkum, P. G., & Franx, M. 2000, ApJ,
  531, 159
Kenyon, S. J., & Bromley, B. C. 2017, ApJ, 850, 50
Kilic, M., Bergeron, P., Kosakowski, A., et al. 2020, ApJ, 898, 84
Klein, B., Blouin, S., Romani, D., et al. 2020, ApJ, 900, 2
Klein, B., Jura, M., Koester, D., Zuckerman, B., & Melis, C. 2010, ApJ,
   709, 950
Li, L., Zhang, F., Kong, X., Han, Q., & Li, J. 2017, ApJ, 836, 71
Liebert, J., Bergeron, P., & Holberg, J. B. 2005, ApJS, 156, 47
Limoges, M. M., Bergeron, P., & Lépine, S. 2015, ApJS, 219, 19
Malamud, U., & Perets, H. B. 2020, MNRAS, 492, 5561
Maldonado, R. F., Villaver, E., Mustill, A. J., Chavez, M., & Bertone, E.
   2020a, MNRAS, 497, 4091
Maldonado, R. F., Villaver, E., Mustill, A. J., Chavez, M., & Bertone, E.
  2020b, MNRAS, 499, 1854
Manser, C. J., Gänsicke, B. T., Eggl, S., et al. 2019, Sci, 364, 66
Manser, C. J., Gänsicke, B. T., Gentile Fusillo, N. P., et al. 2020, MNRAS,
  493, 2127
Manser, C. J., Gänsicke, B. T., Koester, D., Marsh, T. R., & Southworth, J.
  2016a, MNRAS, 462, 1461
Manser, C. J., Gänsicke, B. T., Marsh, T. R., et al. 2016b, MNRAS, 455, 4467
Marshall, J. L., Burles, S., Thompson, I. B., et al. 2008, Proc. SPIE, 7014,
  701454
Matlovič, P., Tóth, J., Kornoš, L., & Loehle, S. 2020, Icar, 347, 113817
McCook, G. P., & Sion, E. M. 1987, ApJS, 65, 603
Melis, C., & Dufour, P. 2017, ApJ, 834, 1
Melis, C., Dufour, P., Farihi, J., et al. 2012, ApJL, 751, L4
Melis, C., Farihi, J., Dufour, P., et al. 2011, ApJ, 732, 90
Melis, C., Jura, M., Albert, L., Klein, B., & Zuckerman, B. 2010, ApJ,
  722, 1078
Metzger, B. D., Rafikov, R. R., & Bochkarev, K. V. 2012, MNRAS, 423, 505
Miranda, R., & Rafikov, R. R. 2018, ApJ, 857, 135
Mustill, A. J., Villaver, E., Veras, D., Gänsicke, B. T., & Bonsor, A. 2018,
   MNRAS, 476, 3939
Nixon, C. J., Pringle, J. E., Coughlin, E. R., Swan, A., & Farihi, J. 2020,
  arXiv:2006.07639
Rafikov, R. R. 2011a, ApJL, 732, L3
Rafikov, R. R. 2011b, MNRAS, 416, L55
Rebassa-Mansergas, A., Solano, E., Xu, S., et al. 2019, MNRAS, 489, 3990
Swan, A., Farihi, J., & Wilson, T. G. 2019, MNRAS, 484, L109
Swan, A., Farihi, J., Wilson, T. G., & Parsons, S. G. 2020, MNRAS, 496, 5233
van Hoof, P. A. M. 2018, Galax, 6, 63
Vanderburg, A., Johnson, J. A., Rappaport, S., et al. 2015, Natur, 526, 546
Veras, D., Leinhardt, Z. M., Bonsor, A., & Gänsicke, B. T. 2014, MNRAS,
Veras, D., Mustill, A. J., Gänsicke, B. T., et al. 2016, MNRAS, 458, 3942
Vogt, S. S., Allen, S. L., Bigelow, B. C., et al. 1994, Proc. SPIE, 2198, 362
Wang, T.-g., Jiang, N, Ge, J, et al. 2019, ApJL, 886, L5
Wilson, D. J., Gänsicke, B. T., Koester, D., et al. 2014, MNRAS, 445, 1878
Wilson, D. J., Gänsicke, B. T., Koester, D., et al. 2015, MNRAS, 451, 3237
Xu, S., Dufour, P., Klein, B., et al. 2019, AJ, 158, 242
Xu, S., & Jura, M. 2014, ApJL, 792, L39
Xu, S., Jura, M., Dufour, P., & Zuckerman, B. 2016, ApJL, 816, L22
Xu, S., Jura, M., Klein, B., Koester, D., & Zuckerman, B. 2013, ApJ, 766, 132
Xu, S., Lai, S., & Dennihy, E. 2020, ApJ, 902, 127
Zuckerman, B., Koester, D., Melis, C., Hansen, B. M., & Jura, M. 2007, ApJ,
Zuckerman, B., Koester, D., Reid, I. N., & Hünsch, M. 2003, ApJ, 596, 477
```

Zuckerman, B., Melis, C., Klein, B., Koester, D., & Jura, M. 2010, ApJ,

722, 725